Development of new generation coatings for enhanced ultrasound imaging

van der Vleuten, C.

Award date:
2020

EINDHOVEN UNIVERSITY OF TECHNOLOGY

Department of Mechanical Engineering
Mechanics of Materials Group

Development of New Generation Coatings for Enhanced Ultrasound Imaging

Master Thesis

C. van der Vleuten

Supervisor:
dr. ir. V.G. Kouznetsova

Committee:
dr. ir. J.A.W. van Dommelen
dr. ir. V.G. Kouznetsova
dr. ir. R.G.P. Lopata
dr. C.M. van Heesch

Eindhoven, April 2020

Abstract

The aim of this study is to investigate novel concepts for a needle coating with an improved ultrasound reflection compared to the currently used needles. A locally resonant acoustic metamaterial (LRAM) coating is designed which is a novel technique in needle coating. The performance of this needle coating is compared to the performance of a needle with a polymer coating containing voids, which is an alternative needle coating in industry. The effectiveness of the different needle setups is evaluated in a numerical model in COMSOL. The comparison shows that a locally resonant acoustic metamaterial provides a better reflection of an ultrasound wave than the coating containing voids, both for a two- and three-dimensional structure. However, the conventional coatings, as well as the LRAM structure do not reflect an incident wave back in the direction of the ultrasound probe when the imaging probe and needle are under an angle. Therefore, the application of a metamaterial with double negative properties is studied as well. These metamaterials can manipulate the refractive angle of an incident wave, but the double negative metamaterial structure in this study is shown not to be suited for the problem at hand, i.e. for realising a negative reflection angle.

Keywords locally resonant acoustic metamaterial, ultrasound image guidance, frequency band diagram, reflection factor, COMSOL multiphysics

Contents

Chapter 1

Introduction

Medical procedures like needle placement, biopsies, stent placements and minimal evasive surgeries are typically performed under guidance of ultrasound imaging. Ultrasound imaging is a technique where high frequency sound waves are used to produce an image of a region of interest inside the body. In Fig. 1.1a an example of ultrasound imaging guidance is depicted; a needle is visualised using an ultrasound imaging probe. The use of the imaging probe eases the determination of the exact position of the medical device, e.g. needle, with respect to its target. However, in practice these medical devices are often difficult to visualise with ultrasound imaging due to the large mismatch between the wave scattering properties of the human tissue and the medical instruments. Especially when it concerns the visualisation of a small medical device like a needle.

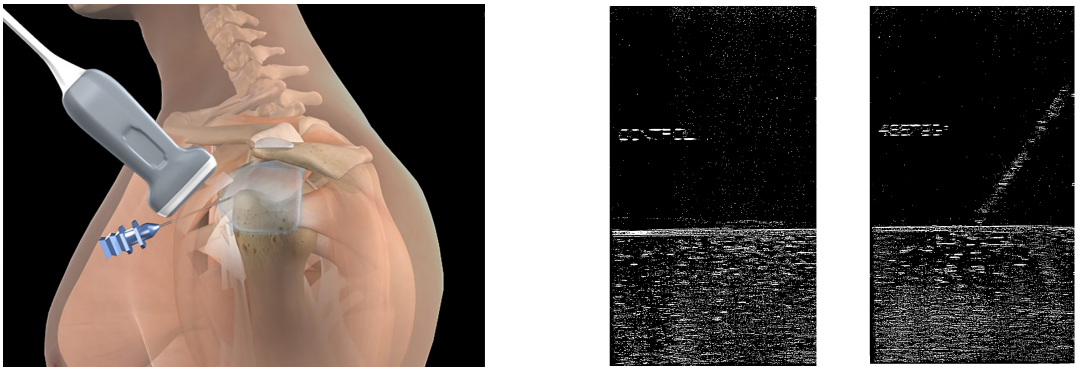

(a) (b)

Figure 1.1: Example of an ultrasound imaging guidance system. a) An ultrasound imaging guidance procedure for a needle placement using an imaging probe [13]. b) Ultrasound image of phantom model of blood and liver; with an uncoated wire (not visible) and coated wire to enhance the visibility [36].

The objective of this study is to improve the visibility of medical devices in ultrasound imaging. With the ultimate goal of developing a new kind of coating for medical devices. In this study the focus is on enhancing the ultrasound visibility of needles. In Fig. 1.1b, two images of a wire are displayed. The first image shows a wire with an untouched surface; this wire is not visible apart from a slight disparity in the lower medium. The second wire is coated with a polymer composite, greatly enhancing the visibility. However, it is not clear where the tip of the coated wire is situated. Therefore the visibility would preferably be improved even further.

The needles currently used in ultrasound imaging guidance have their surfaces treated in a way to optimise the scattering of the ultrasound waves. A common technique is to threat the surface in a similar fashion as for the polymer composite coating on the wire in Fig. 1.1b. The goal of this

study is to investigate novel coating concepts which enhance the reflection even further, especially focusing on coatings with active reflecting properties to optimise the reflection of the ultrasound waves for a certain frequency range. These kind of coatings consist of resonant particles. Such a coating material is referred to as a Locally Resonant Acoustic Metamaterial (LRAM). The coating will be designed to reflect waves with a frequency between $2 - 15$ MHz, since this is the frequency range for which ultrasound imaging guidance for needles is typically performed. Another criteria regards the angle at which the needle is visualised. Needle placement is typically performed with an angle of insertion of $30 - 50$ degrees from normal insertion. The imaging probe will therefore be visualising the needle at this angle as well, meaning that the needle has an angle of $40 - 60$ degrees with the acoustic waves transmitted from the imaging probe.

This study will commence with an overview of the state of the art regarding needle ultrasound visibility techniques in Chapter 2. This will be done by looking into a comparison between different commercially available needles and providing an overview of needle coating patents which are closest to the technique which is proposed in this study. Next the reflection and refraction at different boundaries is studied in Chapter 3. Starting with a study of two liquid domains and gradually complicating the problem to a liquid-solid-solid structure representing a skin-coating-needle structure. For every kind of structure an analytical derivation is provided which is compared to a numerical result in COMSOL. In the following chapter, Chapter 4, the basic working principles of some relevant acoustic metamaterials is provided. This basic information will lead to a more in depth explanation of Locally Resonant Acoustic Metamaterials (LRAMs). In Chapter 5 a LRAM coating design is proposed. For this proposed metamaterial the band diagram of the unit cell is evaluated. Also the performance of the unit cell when implemented in a needle coating is evaluated. The performance of this newly designed coating will be compared to the performance of an ultrasound visibility technique currently applied in the industry. In the last chapter, Chapter 6, the application of a double negative LRAM is evaluated as an attempt to manipulate the reflection angle of an incident wave. Lastly, the conclusions of this report are provided.

Chapter 2

State of the Art

In this chapter the currently used techniques for improving reflection properties of needles are provided. First, different reflection enhancing techniques for needles are compared. Next, patents are highlighted that are the most relevant to exploring LRAM structures. With this information an overview of the current state of needle surface treatments is presented.

2.1 Commercial Needle Comparison

For some medical procedures where a needle is inserted into the body it is important to visualise the exact location of this needle. The tip and shaft of this needle will therefore be visualised by ultrasound imaging, this procedure is called ultrasound image guidance. But due to the small dimensions of the needle, this procedure can sometimes show difficulties. In a study by S-J Tang *et al.* [34], ten commercial needles used for ultrasound imaging were compared to examine what needle demonstrates the best visibility according to medical professionals. In this particular study, medical professionals were asked to rank ten needles in functionality. Since the needle insertion angle in clinical applications is usually between 30 and 50 degrees from normal insertion, these two extremes were examined. In Fig. 2.1, the visibility of three needles under two insertion angles is displayed. In these images it can be seen that the visibility of the shaft and tip can differ greatly for different needles. For some needles the whole shaft including the tip is visible, for others the shaft is less visible and the tip can be distinguished as a single dot.

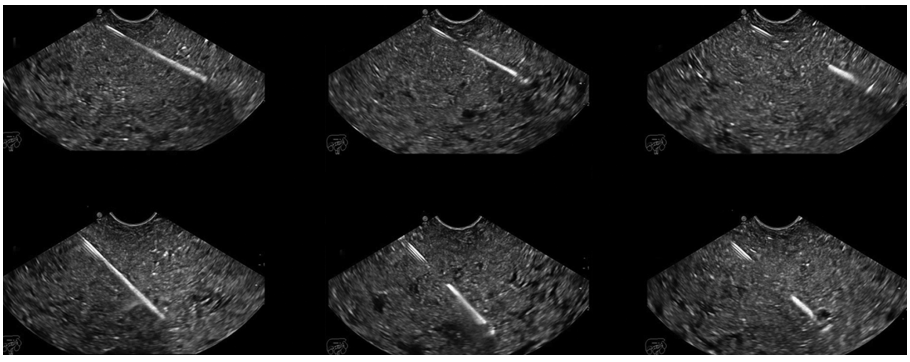

Figure 2.1: Endoscopic ultrasound images of three different needles at insertion angles of 30 and 50 degrees [34].

The visibility of the needle tip is crucial during ultrasound imaging. One method used to improve the visibility of the needle is to treat the surface with techniques such as laser etching, mechanical dimpling, or sandblasting [9]. With these techniques a roughness or pattern is applied to the needle surface causing the incident wave to have an improved scattering. Ultimately

resulting in a larger portion of the incident wave to be reflected back to the imaging probe. A second technique to improve the visibility of the needle is to apply a polymer coating to the needle surface. This coating contains spherical inclusions or voids. These inclusions cause a similar effect; the incident wave scatters on the inclusions, resulting is a highly scattered wave.

During the comparison between the ten needles, the needles with a polymer coating showed to have a good visibility over the entire shaft up to the tip. The visibility of needles with a roughened needle surface was good within the treated segments of the needle. The polymer coated needles were the most desired by the professionals. The exact composition of the polymeric coatings is unfortunately not published by the manufacturers. However, it is evident that a polymer coating is more desirable than a needle with a roughened surface.

2.2 Needle Coating Patents

Different patents are published about enhancing the visibility of needles during ultrasound imaging. The majority of these patents focus on the structural configuration of the coating rather than on the actual materials the coating is composed of. Four patents are selected which are related the closest to the goal of this study; improving the ultrasound wave reflection, references [28, 15, 10, 36]. Every patent will be discussed briefly and will be supported by an image from the patent application:

1. **L. Partika (1995) [28]:** This patent proposes to cover selected areas along the needle with a reflective material. The reflective material consists of gas bubbles contained in a polymeric material, Fig. 2.2a. Due to the large mismatch in impedance between the polymer material and the gas bubbles, this material configuration exhibits high reflectivity of ultrasound waves. The gas bubbles are contained inside the polymer material but are also allowed to form cavities on the surface of the coating. The bubbles can consist of any gas, including air.

2. **M.L. Jones *et al.* (2003) [15]:** For this patent the composite material layer consists of glass microspheres, void spaces or a combination of the two, Fig. 2.2b. These inclusions have a diameter typically ranging from $10\mu m - 100\mu m$. In principle this patent covers the same aspects as the previous patent, except for the fact that hard particles can be included in the composite material. Hard particles can be suitable as well due to the large mismatch in impedance. Another difference is the electrically insulating layer underneath. This layer makes the coating suitable for use with medical devices that are exposed to a high voltage electrical energy, e.g. radio frequency. For this study, such an isolating component is not required.

3. **L.A. Couvillon and T.J. Teo (2005) [10]:** The coating of this patent consists of multiple layers, including a layer containing a contrast agent, Fig. 2.2c. The contrast agent preferably consists of micro bubbles. These respond to the incident ultrasound waves to generate vibrations at the harmonics of the incident wave in the layer. Due to the vibrations, the ultrasound reflection back to the probe is enhanced. This is the only patented coating which mentions the actual generation of vibrations by inclusions, which is also the focus of the present study.

4. **M.R. Violante *et al.* (2007) [36]:** This coating contains voids with entrapped gas, Fig. 2.2d. These irregularities in the polymeric coating cause a better scattering and therefore a better ultrasound image at the probe, similar to patent by L. Partika *et al.*. However, in this patent the gas bubbles are made reactive; only making them visible under certain met circumstances, e.g. a temperature threshold. For this study this is an unnecessary property.

The main characteristic of the four prior art patents is the use of micro-inclusions in the coating. These inclusions can either be gas bubbles or solid particles. For the most part, these particles act as reflectors of the incident ultrasound wave. In the patent by L.A. Couvillon and T.J. Teo however, the generation of vibrations is mentioned. Though, these vibrations are caused at the harmonics of the coating layer, meaning that the coating thickness is more significant than the

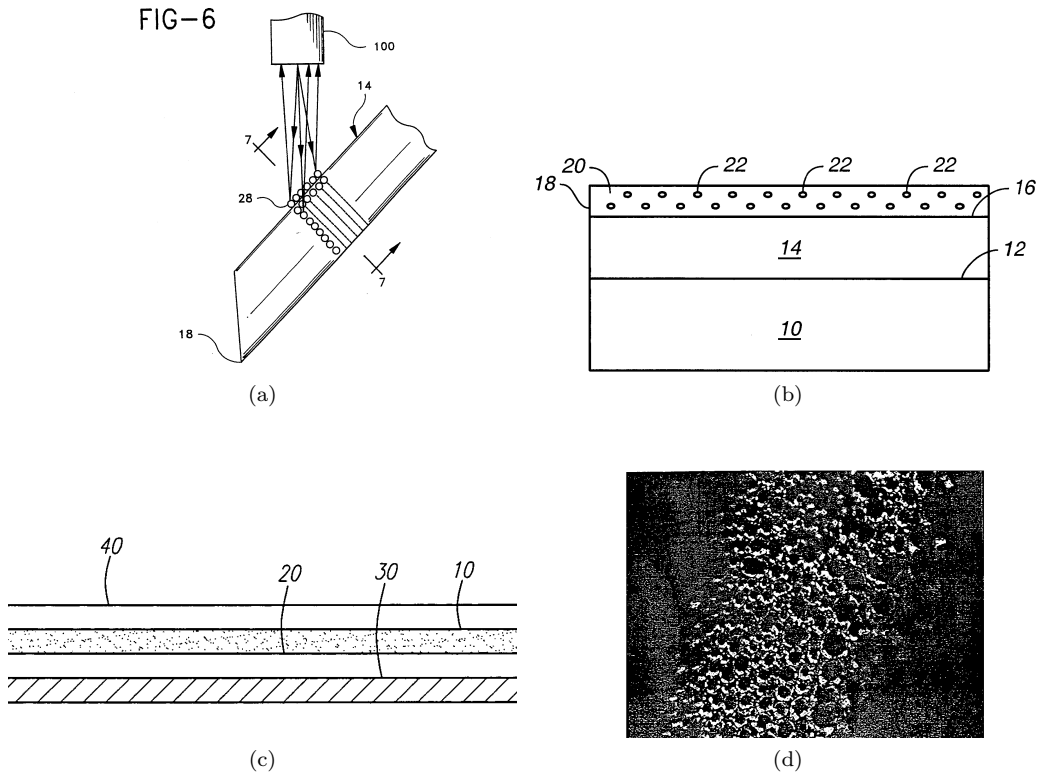

Figure 2.2: Images from four different patents. (a) Patent by Partika [28], sketch of a partially coated needle with gas bubble inclusions. (b) Patent by Jones *et al.* [15], coated substrate consisting of an insulative layer and an echogenic layer including particles, voids or both. (c) Patent by Couvillon and T.J. Teo [10], ultrasound coating consisting of an adhesion layer, ultrasound contrast agent and outer layer. (d) Patent by Violante *et al* [36], microscopic image of a needle with an echogenic coating containing voids.

actual properties of the vibrating particles; this is not a locally resonant acoustic metamaterial. From the current patents on needle coatings for ultrasound purposes it seems to be that the application of locally resonant acoustic metamaterials is so far unstudied.

2.3 Coating with Gas Producing Agent

Another technique to enhance the needle visibility is by using a bubbling agent. In a study by S.M. Tavakoli *et al.* multiple samples were produced making use of this technique to compare their visibility [35]. The gas producing agent in the coating reacts with the tissue fluid as the needle penetrates. This chemical reaction produces gas bubbles on the surface of the coating. These bubbles will have the same effect as encapsulated voids in a coating; enhance the ultrasound scattering. The working principle is different from the patent by M.R. Violante *et al.*; here the bubbles were formed on the coating surface, where in the patent the bubbles are formed within the coating layer. There is no documentation whether this technique is applied in commercially available needles. The needle samples were examined under ultrasound in a tissue-mimicking material, with acoustic properties similar to those of soft tissue.

2.4 Overview

By examining the currently available needles, it is clear that many technologies exist to enhance the ultrasound imaging visibility of needles. Currently, the best visibility is obtained from needles with a polymeric coating containing voids. By reviewing the patents and experiments for medical coatings, this polymer coating seems to be the latest and best on the market.

As far as known, there is no patent history on using resonating particles in needle coatings to enhance ultrasound visibility. This leaves a promising opening for the investigation of LRAM needle coatings, which will be exploited in the present work.

Chapter 3

Incident Pressure Wave

In this chapter the propagation of ultrasound waves in a liquid and solid medium is studied. First, the wave properties in a medium are derived. Next, the reflected and transmitted wave energies and angles are calculated for different structures of media, starting with a liquid-liquid interface and gradually complicating the problem towards a liquid-solid-solid interface, representing the skin-coating-needle problem of this study. For every structure the result from an analytical derivation is presented and compared to the results obtained from a numerical finite element model in COMSOL.

3.1 Acoustic Pressure Waves

There are two types of waves that can travel in a medium; an acoustic longitudinal/pressure wave and a shear wave. In a liquid it is not possible for shear waves to appear. Therefore, it can be assumed that a liquid can be described by only a pressure wave. Shear waves will come into consideration once solid media are introduced, for now the focus will be on pressure waves only. First, the balance of momentum is considered:

$$\vec{\nabla} \cdot \boldsymbol{\sigma} + p\vec{q} = \rho\dot{\vec{v}}, \tag{3.1}$$

where $\vec{\nabla} \cdot \boldsymbol{\sigma}$ indicates the divergence of the stress tensor, $p\vec{q}$ is the pressure contribution due to body forces and $\rho\dot{\vec{v}}$ is the density multiplied by the time derivative of the velocity. Since the body forces are not present in the current problem description, the equation can be reduced to:

$$\vec{\nabla} \cdot \boldsymbol{\sigma} = \rho\dot{\vec{v}}. \tag{3.2}$$

Now, the stress tensor $\boldsymbol{\sigma}$ is considered. As a definition the stress tensor can be written as:

$$\boldsymbol{\sigma} = -p\boldsymbol{I} + \boldsymbol{\tau}, \tag{3.3}$$

where $\boldsymbol{I}$ is the unity tensor and $\boldsymbol{\tau}$ is the shear stress tensor. Since it is assumed that shear forces are not present in the liquid, the equation can be reduced to:

$$\boldsymbol{\sigma} = -p\boldsymbol{I}. \tag{3.4}$$

The substitution of Eq. (3.4) into Eq. (3.2) result in the following relation:

$$-\vec{\nabla}p = \rho\dot{\vec{v}}. \tag{3.5}$$

Instead of considering a velocity vector $\vec{v}$, a velocity potential ϕ is defined in such a way that $\vec{v} = \vec{\nabla}\phi$ [33]. This means the derivative with respect to time can be expressed as:

$$\dot{\vec{v}} = \frac{\partial\vec{\nabla}\phi}{\partial t}, \tag{3.6}$$

where t denotes time. This new expression for $\dot{\vec{v}}$ can be implemented in Eq. (3.5):

$$\begin{aligned} -\vec{\nabla}p &= \rho\frac{\partial\vec{\nabla}\phi}{\partial t}, \\ -p &= \rho\frac{\partial\phi}{\partial t}. \end{aligned} \tag{3.7}$$

Now the definition of the wave equation is needed. The one dimensional wave equation for a wave travelling in the direction of the spatial coordinate z can be written as [33]:

$$\frac{\partial^2\phi}{\partial z^2} - \frac{1}{c^2}\frac{\partial^2\phi}{\partial t^2} = 0, \tag{3.8}$$

where the parameter c is the velocity of the wave. The wave velocity can be derived when another derivation using Newton's second law and Hooke's law is considered. This derivation can be found in App. A.1. The longitudinal wave c_L and shear wave c_S have different propagating velocities:

$$\begin{aligned} &\text{Liquid medium:} && c_L = \left(\frac{K}{\rho}\right)^{\frac{1}{2}}, \\ &\text{Solid medium:} && c_L = \left(\frac{K+\frac{4}{3}\mu}{\rho}\right)^{\frac{1}{2}}, && c_S = \left(\frac{\mu}{\rho}\right)^{\frac{1}{2}}, \end{aligned} \tag{3.9}$$

where K and μ represent the bulk and shear modulus of the medium respectively. The longitudinal wave velocity is in fact similar for the liquid and solid media: the absence of a shear modulus, μ, in the liquid medium simplifies c_L to the equation for a liquid medium.

In Eq. (3.8) the right velocity can be implemented. Also the velocity potential will be replaced with the expression of Eq. (3.7) and the definition $\vec{v} = \vec{\nabla}\phi$:

$$\begin{aligned} v^2 - \frac{1}{c_L^2}\left(\frac{-p}{\rho}\right)^2 &= 0, \\ v^2 - \frac{p^2}{c_L^2\rho^2} &= 0, \\ v - \frac{p}{c_L\rho} &= 0. \end{aligned} \tag{3.10}$$

This equation leads to a measure referred to as the characteristic impedance Z: a ratio of a forward travelling longitudinal wave to the particle velocity in the fluid [33]:

$$Z_L = \frac{p}{v_L} = \rho c_L. \tag{3.11}$$

This characteristic impedance is a measure of the resistance of the wave in the medium. At interfaces, calculations with the characteristic velocities and characteristic impedance of every medium allow for determination of refraction/reflection angles and transmitted/reflected amplitudes of an incident pressure wave.

3.2 Two Layer Liquid Interface

The equations for pressure waves are now applied to a two layer liquid interface. First the analytical solution will be derived. Then, this analytical solution will be used to confirm a numerical model for a similar problem constructed in COMSOL.

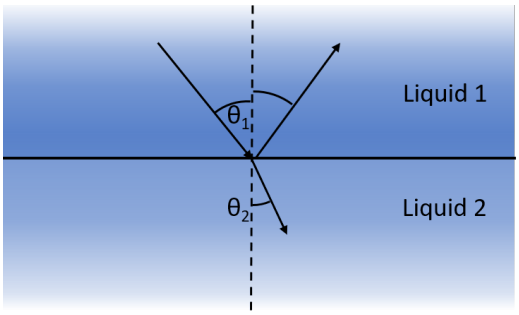

Figure 3.1: Schematic representation of a wave hitting a two layer liquid interface.

3.2.1 Analytical Derivation

When a two layer liquid interface is considered, the incident wave will result in a reflected and refracted longitudinal pressure wave. A schematic representation of this problem can be found in Fig. 3.1. It is assumed that the two layers are infinite in length and width. The absence of these boundaries results in an independence on the frequency of the incident wave. The angle of the resulting waves can be determined using Snell's law, relating the longitudinal velocity of the wave to the angle [16]:

$$\frac{\sin\theta^{(1)}}{\sin\theta^{(2)}} = \frac{c_L^{(1)}}{c_L^{(2)}}, \tag{3.12}$$

where θ indicates the angle between the longitudinal wave and the interface normal. The numbers $^{(1)}$ and $^{(2)}$ refer to the incident and resulting wave respectively. For the determination of the amplitudes of the two resulting waves, the effective impedances of the two considered media are needed. The effective impedance is the impedance normal to the interface [33]:

$$Z^{(i)} = \frac{\rho^{(i)} c_L^{(i)}}{\cos\theta^{(i)}} = \frac{Z_L^{(i)}}{\cos\theta^{(i)}}, \tag{3.13}$$

where $Z^{(i)}$ indicates the impedance in the normal direction and i refers to the wave that is considered. Now the interface problem is considered; an incident pressure wave with pressure $p^{(1)}$ hits the interface and creates a reflected wave with pressure $p^{(0)}$ and a refracted wave with pressure $p^{(2)}$. The reflected and refracted wave have an amplitude related to $p^{(1)}$ by factors RF and TF respectively. Since the pressure needs to be balanced, $p^{(2)}$ can be presented by:

$$p^{(2)} = p^{(1)}\left(1 + RF\right). \tag{3.14}$$

The particle velocity in the second medium can be expressed using the characteristic impedance of Eq. (3.11), but the pressure will still be expressed as the sum of the two pressure waves in the first medium:

$$v^{(2)} = \frac{p^{(2)}}{Z^{(2)}} = \frac{\left(1 - RF\right)p^{(1)}}{Z^{(1)}}. \tag{3.15}$$

Now, by using Eqs. (3.14) and (3.15), the impedance of the second medium can be written as:

$$Z^{(2)} = \frac{p^{(2)}}{v^{(2)}} = \frac{\left(1 + RF\right)Z^{(1)}}{1 - RF}. \tag{3.16}$$

This equation can be rewritten to get an equation for the reflection factor (RF) and transmission factor (TF) of a two layer liquid interface [33]:

$$RF = \frac{Z^{(2)} - Z^{(1)}}{Z^{(1)} + Z^{(2)}}, \tag{3.17}$$

and with $TF = 1 + RF$:

$$TF = \frac{2Z^{(2)}}{Z^{(1)} + Z^{(2)}}. \tag{3.18}$$

3.2.2 Numerical Model Verification

The equations derived previously are solved for a pressure wave hitting a skin-coating interface and for a pressure wave hitting a coating-skin interface. The material properties used for this evaluation can be found in Table 3.1 [25]. The longitudinal and shear wave velocities of the media are determined using Eq. (3.9). Since both media are assumed to be a liquid in the current setup, only the longitudinal wave can propagate. This exact problem is also modelled in COMSOL. A sketch of this model is provided in Fig. 3.2. A pressure field is applied on the first medium to mimic a propagating pressure wave. This applied pressure wave has a certain angle of incident θ on the interface between medium 1 and 2. On the two ends of this structure, a Perfectly Matched Layer (PML) is applied. These layers mathematically dampen incident waves, which means that no energy will reflect from these domains. Due to these layers the domains of media 1 and 2 can be assumed to be infinitely long. On the sides of the model, highlighted in red in Fig. 3.2, Floquet-Bloch periodicity is applied. This boundary condition provides preservation of the periodicity of the travelling waves in the medium, while accounting for periodicity of the structure itself as well. By applying this periodicity, the domains can be assumed to be infinitely wide as well, eliminating any boundary effects on the evaluated structure. In the out of plane direction plane strain is assumed.

Table 3.1: Material properties of skin, polyethylene and stainless steel used for the interface problems.

Material	c_L $[m/s]$	c_S $[m/s]$	ρ $[kg/m^3]$	E $[Pa]$	ν $[-]$
Human tissue (skin) [25]	1615	–	1090	–	–
Polyethylene (coating)	1452	438	900	$0.5 \cdot 10^9$	0.45
Stainless steel (needle)	5302	2976	8000	$180 \cdot 10^9$	0.27

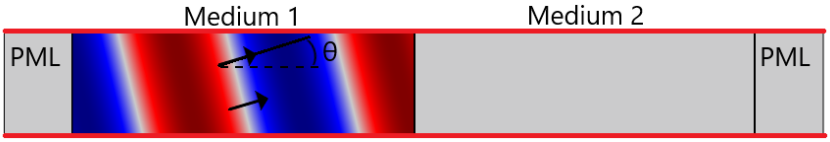

Figure 3.2: Visualisation of a two layer model setup for the numerical model verification in COMSOL.

The comparison of the analytical and numerical results are displayed in Fig. 3.3. In Figs. 3.3a-3.3c, a skin-coating structure is assumed with the pressure field applied to the skin layer. In Figs. 3.3d-3.3f, a coating-skin structure is assumed, which means that the pressure field is applied to the coating layer. The examined parameters are the refraction angle, RF and TF for the first, second and third figure respectively, all as a function of the incident angle. The overall conclusion from this comparison is that there is a great similarity between the analytical and numerical results. For the skin-coating interface, the results are completely similar for all three of the examined parameters. For the coating-skin interface, there is a mismatch in the results for large incident angles. In this case the refraction angle is larger than the incident angle, for large incident angles this results in the refraction angle approaching the interface surface (an angle of $\pi/2$ rad). This results in a more complex result, beyond the analytical solution presented here. To summarise, the numerical model gives correct results for a simple two layer liquid interface problem.

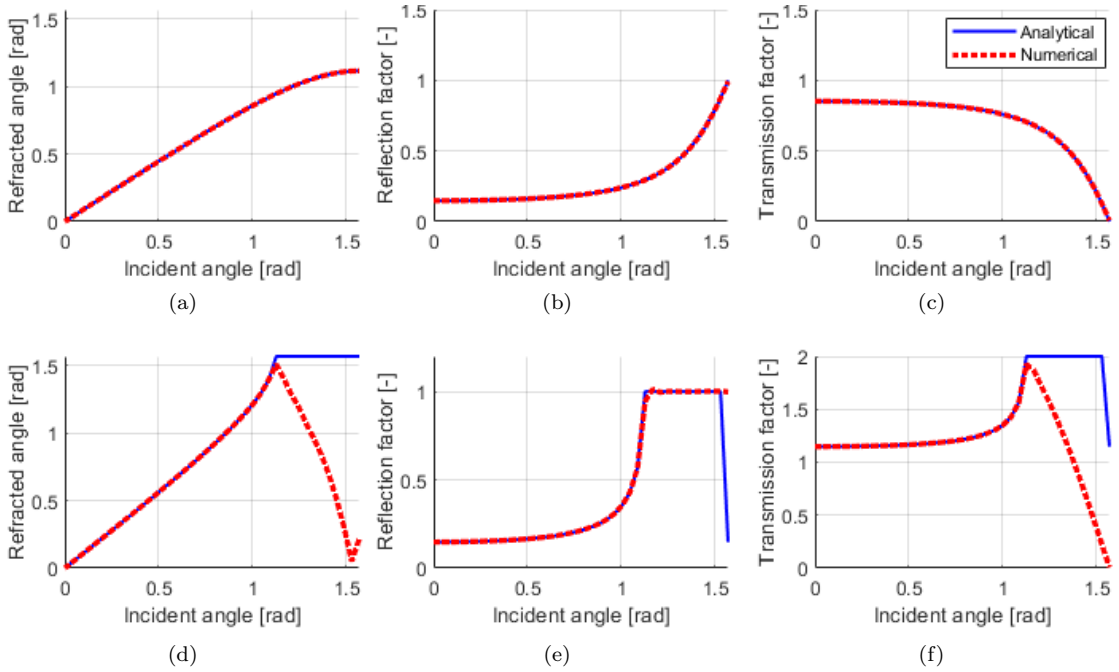

Figure 3.3: Analytical and numerical solution of the refraction angle (first column), reflection factor (second column) and transmission factor (third column) as a function of the incident angle for a wave hitting a two layer liquid interface. (a-c): Pressure wave in skin hitting a coating interface. (d-f): Pressure wave in coating hitting a skin interface.

3.3 Three Layer Liquid Interface

When a three layer liquid interface problem is concerned, unlike the previous problem, the solution is dependent on the frequency of the pressure wave. In the previous problem, there is no frequency dependency since the two layers are assumed to be infinitely long and wide. As soon as the length of a layer is finite, a frequency dependency emerges. This dependency will be examined by considering a three layer liquid structure of infinite width and a middle medium of finite length. Meaning the assumption that only longitudinal pressure waves propagate still holds (liquid). First, this problem will be solved analytically. Then, this problem will be solved numerically and compared to the analytical solution for verification.

3.3.1 Analytical Derivation

For a three layer liquid interface the wave hitting the second interface will also result in a reflected and refracted wave. Resulting in a more complex relationship for the reflection and transmission factors. A schematic representation of this problem can be seen in Fig. 3.4. The middle layer is assumed to have a finite length d, whereas the two outer layers will be infinitely long. The angles of the resulting waves can again be calculated by making use of Snell's law:

$$\frac{\sin\theta^{(1)}}{\sin\theta^{(2)}} = \frac{c_L^{(1)}}{c_L^{(2)}} \qquad \text{and} \qquad \frac{\sin\theta^{(2)}}{\sin\theta^{(3)}} = \frac{c_L^{(2)}}{c_L^{(3)}}. \tag{3.19}$$

To calculate the reflection and transmissions factors for this three layer problem, the reflection and refraction factors calculated in the two layer interface problem are used, Eqs. (3.17) and (3.18). The reflection factor for the three layer problem consists of multiple wave paths. (1) The incident wave is reflected from interface 1-2. (2) The incident wave is transmitted through interface 1-2,

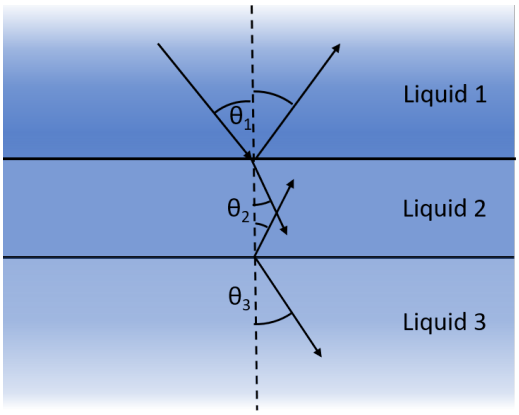

Figure 3.4: Schematic representation of a wave hitting a three layer liquid interface.

then reflects from interface 2-3 and finally refracts through interface 1-2. (3) The incident wave is transmitted through interface 1-2, then reflects from interface 2-3, 1-2, 2-3 and then transmits through interface 1-2. And so on. The amplitudes corresponding to these wave paths can be expressed as [5]:

$$\begin{aligned} &(1) \quad RF_{12}, \\ &(2) \quad TF_{12}RF_{23}TF_{21}e^{2ik_n^{(2)}d}, \\ &(3) \quad TF_{12}RF_{23}RF_{21}RF_{23}TF_{21}e^{4ik_n^{(2)}d}, \end{aligned} \tag{3.20}$$

where $k_n^{(2)}$ represents the wave number in the second medium in the normal direction to the interface. This exponential factor takes change in phase of the wave in the second medium into account. A measure for RF consists of a sum of all the relevant wave paths and can be written as:

$$RF = RF_{12} + TF_{12}RF_{23}TF_{21}e^{2ik_n^{(2)}d}\sum_{n=0}^{\infty}\left[RF_{23}RF_{21}e^{2ik_n^{(2)}d}\right]^n, \tag{3.21}$$

which can be rewritten when the formula for an infinite geometric progression is used [1]:

$$RF = RF_{12} + \frac{TF_{12}RF_{23}TF_{21}e^{2ik_n^{(2)}d}}{1 - RF_{23}RF_{21}e^{2ik_n^{(2)}d}}. \tag{3.22}$$

The transmission factor for a three layer liquid structure can be determined in a similar manner. The first wave path is a direct transmission though the two interfaces. The second path is a wave propagating through the first interface, then reflecting on the boundary twice (RF_{23} & RF_{21}) and then propagating through the 2-3 interface. The following wave paths will show an equal path except for an increasing number of reflections between the two interfaces while travelling in middle medium. The first three transmitted waves paths are expressed as:

$$\begin{aligned} &(1) \quad TF_{12}TF_{23}, \\ &(2) \quad TF_{12}RF_{23}RF_{21}TF_{23}e^{2ik_n^{(2)}d}, \\ &(3) \quad TF_{12}RF_{23}RF_{21}RF_{23}RF_{21}TF_{23}e^{4ik_n^{(2)}d}. \end{aligned} \tag{3.23}$$

The total transmission factor is the sum of all possible wave paths and their amplitudes, resulting in:

$$TF = TF_{12}TF_{23} + TF_{12}RF_{23}RF_{21}TF_{23}e^{2ik_n^{(2)}d}\sum_{n=0}^{\infty}\left[RF_{23}RF_{21}e^{2ik_n^{(2)}d}\right]^n, \tag{3.24}$$

which can be rewritten when a for an infinite geometric progression is used:

$$TF = TF_{12}TF_{23}\frac{TF_{12}RF_{23}RF_{21}TF_{23}e^{2ik_n^{(2)}d}}{1 - RF_{23}RF_{21}e^{2ik_n^{(2)}d}}. \tag{3.25}$$

3.3.2 Numerical Model Verification

The equations derived for RF and TF are solved for a skin-polymer-needle interface. It is assumed that only longitudinal pressure waves can propagate in the materials. The material properties used for this evaluation, c_L and ρ, can be found in Table 3.1. This exact problem is also modelled in COMSOL, the model setup of this problem is visualised in Fig. 3.5. For this evaluation, the same boundary conditions as for the two layer liquid COMSOL model are used. The only difference is that an extra domain is added. This second domain has a finite length of d, as indicated in the figure.

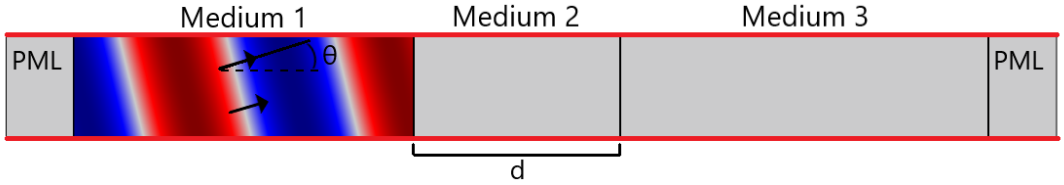

Figure 3.5: Visualisation of a three layer model setup for the numerical model verification in COMSOL.

3.3.2.1 Skin-Coating-Needle

For the skin-coating-needle problem, a comparison of the analytical and numerical reflection and transmission factors for three different incident angles as a function of the frequency can be found in Fig. 3.6. The factors are calculated for a middle layer with length $d = 50$ μm and an incident angle of 0 rad, $\frac{1}{20}\pi$ rad and $\frac{2}{20}\pi$ rad.

For the incident wave with angle $\frac{2}{20}\pi$ rad the reflection is 1. This is due to the large difference in wave velocity between the skin and steel layer. Snell's law can be applied to evaluate the maximum angle for which propagation of a pressure wave in the steel medium is possible. This will be the incident angle for which the propagating wave in the steel medium is approaching $\theta = \frac{\pi}{2}$. When the incident angle exceeds this maximum angle, a maximum reflection will occur. The maximum angle for a skin-coating-steel interface is:

$$\frac{\sin\theta^{(1)}}{\sin\theta^{(2)}} = \frac{c_L^{(1)}}{c_L^{(2)}} \quad \rightarrow \quad \theta^{(1)} = \sin^{-1}\left(\frac{c^{(1)}}{c^{(2)}}\sin\left(\frac{\pi}{2}\right)\right) \approx 0.098\pi \text{ rad}, \tag{3.26}$$

which means that the incident angle of $\frac{2}{20}\pi$ is just too large to get a longitudinal wave propagating in the steel layer, which can also be seen from Fig. 3.7c.

Another observation in Fig. 3.6 is that for different incident angles the peaks for RF and TF are at slightly different frequencies. The dips in the reflection factor are caused by the harmonics of the wave in the middle layer. When half the wavelength fits in the middle layer, this will work as a standing wave. With the node of the wavelength on the interface between the second and third layer. This will result in a decrease in reflection. The frequency for which this phenomenon is observed changes for a different incident angle because the wavelength normal to the boundary, λ_n, will be longer than the wavelength of the propagating wave itself, λ. This means a higher frequency is needed to reduce the size of the wave to match the middle layer. The first dip in the reflection factor occurs at the frequency where:

$$d = \frac{1}{2}\lambda_{L,n} = \frac{\lambda_L}{2\cos\theta} = \frac{c_L}{2f\cos\theta}. \tag{3.27}$$

The wavelength of this longitudinal wave is expressed as: $\lambda_L = \frac{c_L}{f}$, where f represents the frequency in [Hz]. At multiples of this resonance frequency, the higher order harmonics occur. At an angle of 0 rad the first dip should be at 14.5 MHz according to this equation, which is in line with the results.

Fig. 3.7 shows the pressure field resulting from an incident wave with a frequency of 14.5 MHz is visualised for three different angle of incident. Due to the difference in impedance of the first and third material domain, the wavelength and rotated angle is different. It can also be seen that half a wavelength fits the middle layer, which is expected when using Eq. (3.27). When the incident wave is rotated beyond the point where an longitudinal wave can be refracted into the third domain, no wave will occur. Instead a wave at the interface is seen which attenuates further into the third domain. Besides the large deflection of an incident wave, the large difference is longitudinal wave velocity between the different media can be seen as well.

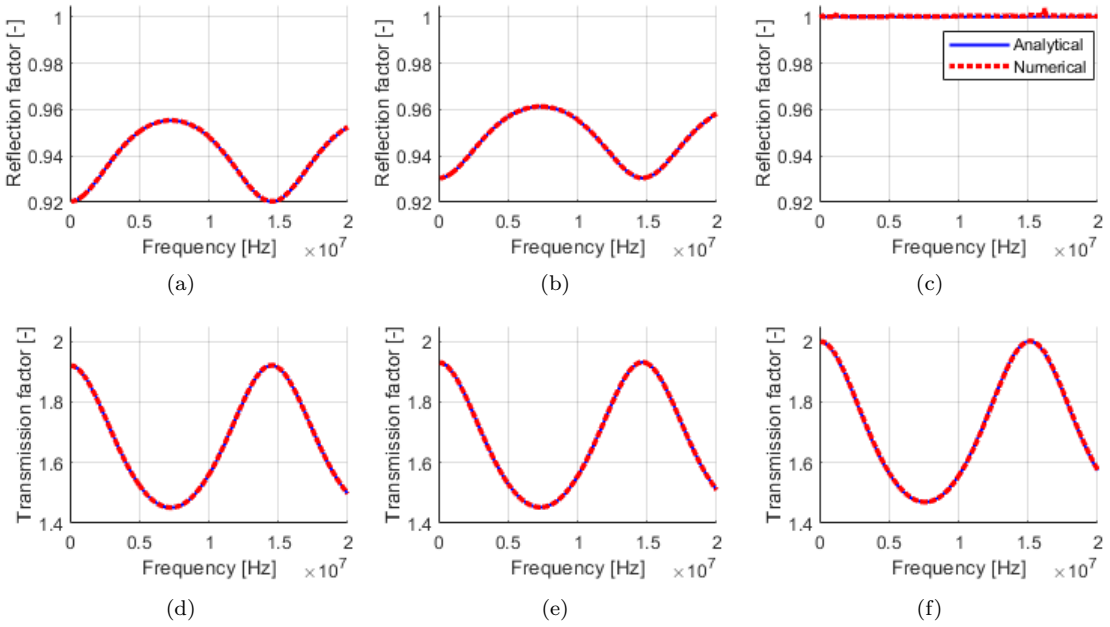

Figure 3.6: Skin-coating-needle problem, modelled as three liquids. Analytical and numerical solution of the reflection and transmission factors as a function of the incident wave frequency. (a-c): Reflection factor for a wave with incident angle of 0 rad, $\frac{1}{20}\pi$ rad and $\frac{2}{20}\pi$ rad respectively. (d-f): Transmission factor for a wave with incident angle of 0 rad, $\frac{1}{20}\pi$ rad and $\frac{2}{20}\pi$ rad respectively.

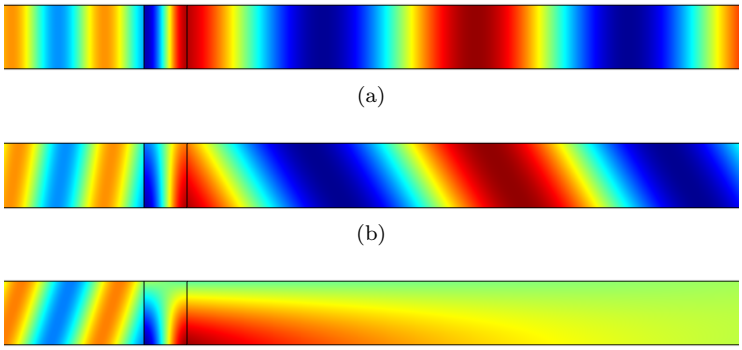

(a) (b) (c)

Figure 3.7: Pressure field resulting from an incident wave in a skin-coating-needle problem, modelled as three liquids at 14.5 MHz. For an incident wave with angle of a) 0 rad. b) $\frac{1}{20}\pi$ rad. c) $\frac{2}{20}\pi$ rad.

3.4 Liquid-Solid Interface

In this section a liquid-solid interface is concerned. This is a more complex structure than the two layer liquid interface since shear waves can propagate in an elastic solid medium as well; causing longitudinal waves and shear waves. First the analytical solution of this problem will be derived. This analytical solution will be used to confirm a numerical model for a similar problem constructed in COMSOL.

3.4.1 Analytical Derivation

For a liquid-solid interface, the incident longitudinal wave will result in a reflected longitudinal wave, a refracted longitudinal wave and a refracted shear wave, visualised in Fig. 3.8. Since the speed of every kind of wave is known, the angles of the three resulting waves can be determined using Snell's law:

$$\frac{\sin\theta_L^{(1)}}{\sin\theta_L^{(2)}} = \frac{c_L^{(1)}}{c_L^{(2)}} \quad \text{and} \quad \frac{\sin\theta_L^{(1)}}{\sin\theta_S^{(2)}} = \frac{c_L^{(1)}}{c_S^{(2)}}. \tag{3.28}$$

The suffixes $_L$ and $_S$ refer to the longitudinal and shear wave respectively. To calculate the reflection and transmission factors at a liquid-solid interface, the analytical derivation by L.M. Brekhovskikh is used [5]. For this derivation the continuity of the boundary is considered. Stating that the sum from all waves should be zero on the boundary for the components of the impedance and displacement:

$$\sum Z_x = 0, \qquad \sum Z_z = 0, \qquad \sum u_z = 0. \tag{3.29}$$

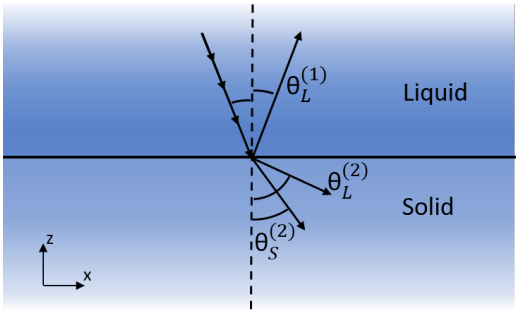

Figure 3.8: Schematic representation of a wave hitting a liquid-solid interface.

The displacement in x-direction is supposed to be free to allow for the liquid medium to slide past the solid domain. The boundary conditions can be expressed in terms of ϕ and ψ, the wave potentials of the longitudinal and shear wave respectively. Resulting in the following boundary conditions, in the same order as Eq. (3.29) [5]:

$$\sum \frac{\rho^{(1)}}{k_S^{(2)2}} \left(\frac{\partial \phi}{\partial z} - ip\psi \right) = 0, \qquad \sum \frac{\rho^{(1)}}{k_S^{(2)2}} \left(\frac{\partial \psi}{\partial z} - ip\phi \right) = 0, \qquad \sum \left(\frac{\partial \phi}{\partial z} - i\xi\psi \right) = 0, \quad (3.30)$$

with

$$p^{(2)} = \frac{\xi^2 - k_S^{2(2)}/2}{\xi}. \quad (3.31)$$

In these equations $k_S^{(2)}$ is the wavenumber of the shear wave in the second medium. The parameter ξ is the horizontal component of the wave number of the incident wave, and is dependent on the angle of incident. The potentials ϕ and ψ, of the longitudinal and shear wave in every layer can be written as [5]:

$$\begin{aligned} \phi &= \phi' e^{i\alpha z} + \phi'' e^{-i\alpha z}, \qquad \text{where } \alpha = \sqrt{k_L^2 - \xi^2}, \qquad k_L = \frac{\omega}{c_L}, \\ \psi &= \psi' e^{i\beta z} + \psi'' e^{-i\beta z}, \qquad \text{where } \beta = \sqrt{k_S^2 - \xi^2}, \qquad k_S = \frac{\omega}{c_S}, \end{aligned} \quad (3.32)$$

where ϕ' and ψ' are the amplitudes of the reflected longitudinal and shear wave respectively, ϕ'' and ψ'' are the amplitudes of the incident longitudinal and shear wave respectively. In the liquid medium, medium 1, shear waves are not supported, resulting in $\psi^{(1)} = 0$. For a wave propagating in a liquid medium incident on a solid boundary, three waves will be produced; a reflected longitudinal wave, a refracted longitudinal wave and a refracted shear wave:

$$\begin{aligned} \text{liquid,} \qquad & \phi^{(1)} = \phi'^{(1)} e^{i\alpha^{(1)} z} + \phi''^{(1)} e^{-i\alpha^{(1)} z}, \\ \text{solid,} \qquad & \phi^{(2)} = \phi'^{(2)} e^{i\alpha^{(2)} z} + \phi''^{(2)} e^{-i\alpha^{(2)} z}, \\ & \psi^{(2)} = \psi'^{(2)} e^{i\beta^{(2)} z} + \psi''^{(2)} e^{-i\beta^{(2)} z}. \end{aligned} \quad (3.33)$$

Now the equations from Eq. (3.33) are substituted in the boundary conditions of Eq. (3.30). This will result in the following three conditions:

$$\begin{aligned} \frac{k_S^{2(2)} \rho^{(1)}}{2\rho^{(2)} \xi} (\phi'^{(1)} + \phi''^{(1)}) + p^{(2)} (\phi'^{(2)} + \phi''^{(2)}) - \beta^{(2)} (\psi'^{(2)} - \psi''^{(2)}) &= 0, \\ \alpha^{(2)} (\phi'^{(2)} - \phi''^{(2)}) + p^{(2)} (\psi'^{(2)} + \psi''^{(2)}) &= 0, \\ \alpha^{(1)} (\phi'^{(1)} - \phi''^{(1)}) - \frac{k_S^{2(2)}}{2\xi} (\psi'^{(2)} + \psi''^{(2)}) &= 0. \end{aligned} \quad (3.34)$$

Since the incident wave originates from the liquid medium, there are no reflected waves in the solid medium: $\phi'^{(2)} = 0$ and $\psi'^{(2)} = 0$. The reflection and transmission factors can now easily be calculated to be: $RF = \phi'^{(1)}/\phi''^{(1)}$, $TF_L = \phi''^{(2)}/\phi''^{(1)}$ and $TF_S = \psi''^{(2)}/\phi''^{(1)}$. This can filled in into Eq. (3.34) and solved for the factors:

$$\begin{aligned} RF &= \frac{4\frac{\rho^{(2)}}{\rho^{(1)}} \alpha^{(1)} \xi^2 (\alpha^{(2)} \beta^{(2)} + p^{2(2)}) - \alpha^{(2)} k_S^{4(2)}}{4\frac{\rho^{(2)}}{\rho^{(1)}} \alpha^{(1)} \xi^2 (\alpha^{(2)} \beta^{(2)} + p^{2(2)}) + \alpha^{(2)} k_S^{4(2)}}, \\ TF_L &= -\frac{4\alpha^{(1)} p^{(2)} \xi k_S^{2(2)}}{4\frac{\rho^{(2)}}{\rho^{(1)}} \alpha^{(1)} \xi^2 (\alpha^{(2)} \beta^{(2)} + p^{2(2)}) + \alpha^{(2)} k_S^{4(2)}}, \\ TF_S &= \frac{\alpha^{(2)}}{p^{(2)}} TF_L. \end{aligned} \quad (3.35)$$

Now the definitions of the impedance, Eq. (3.11), can be used to simplify these equations, resulting in the final equations for RF, TF_L and TF_S:

$$\begin{aligned} RF &= \frac{Z_L^{(2)}\cos^2 2\theta_S^{(2)} + Z_S^{(2)}\sin^2 2\theta_S^{(2)} - Z_L^{(1)}}{Z_L^{(2)}\cos^2 2\theta_S^{(2)} + Z_S^{(2)}\sin^2 2\theta_S^{(2)} + Z_L^{(1)}}, \\ TF_L &= \frac{\rho^{(1)}}{\rho^{(2)}} \cdot \frac{2Z_L^{(2)}\cos 2\theta_S^{(2)}}{Z_L^{(2)}\cos^2 2\theta_S^{(2)} + Z_S^{(2)}\sin^2 2\theta_S^{(2)} + Z_L^{(1)}}, \\ TF_S &= -\frac{\rho^{(1)}}{\rho^{(2)}} \cdot \frac{2Z_S^{(2)}\sin 2\theta_S^{(2)}}{Z_L^{(2)}\cos^2 2\theta_S^{(2)} + Z_S^{(2)}\sin^2 2\theta_S^{(2)} + Z_L^{(1)}}. \end{aligned} \tag{3.36}$$

3.4.2 Numerical Model Verification

The equations derived previously are solved for a pressure wave hitting a skin-needle interface. The material properties used for this evaluation can be found in Table 3.1. The model used in COMSOL is an equivalent to the model used to evaluate the two layer liquid interface sketched in Fig. 3.2. In this sketch the second liquid medium is replaced by a solid medium, there are no additional changes in the model. In COMSOL, the reflection factor can be determined from the resulting pressure wave. Since it is not possible to retrieve the transmission factors in the solid medium directly from COMSOL, a different approach is used to get the two transmission factors. The pressure in the solid medium can be expressed as a function of the displacement field. The total displacement in the solid medium is a combination of the longitudinal and shear wave fields and can be decomposed using the Helmholtz decomposition, where the total displacement field $\vec{U}$ is expressed as [2]:

$$\vec{U} = \vec{\nabla}\phi + \vec{\nabla} \times \vec{\psi}, \tag{3.37}$$

where ϕ and $\vec{\psi}$ are the Helmholtz potentials. The first term represents the longitudinal wave (L) and the second the shear wave (S). Since the longitudinal wave is divergence free and in an isotropic medium, the divergence and curl operators can be applied to Eq. (3.37) [32]:

$$\begin{aligned} L &= \vec{\nabla} \cdot \vec{\nabla}\phi, \\ \vec{S} &= \vec{\nabla} \times \left(\vec{\nabla} \times \vec{\psi}\right). \end{aligned} \tag{3.38}$$

and when a 2D problem is considered, the equations for L and S can be simplified to:

$$\begin{aligned} L &= \partial U_x/\partial x + \partial U_y/\partial y, \\ S &= \partial U_x/\partial y - \partial U_y/\partial x. \end{aligned} \tag{3.39}$$

These values represent strains, and can therefore easily be rewritten to a measure for the stress due to this strain, using the elasticity tensor for elastic isotropic materials in plane strain C^4:

$$\begin{aligned} \begin{bmatrix} \sigma_{11} \\ \sigma_{22} \\ \sigma_{12} \end{bmatrix} &= C^4 \begin{bmatrix} \epsilon_{11} \\ \epsilon_{22} \\ \epsilon_{12} \end{bmatrix} \\ \begin{bmatrix} \sigma_{11} \\ \sigma_{22} \\ \sigma_{12} \end{bmatrix} &= \frac{E}{(1+\nu)(1-2\nu)} \begin{bmatrix} 1-\nu & \nu & 0 \\ \nu & 1-\nu & 0 \\ 0 & 0 & \frac{1-2\nu}{2} \end{bmatrix} \begin{bmatrix} \epsilon_{11} \\ \epsilon_{22} \\ \epsilon_{12} \end{bmatrix} \end{aligned} \tag{3.40}$$

in this equation, L is the longitudinal strain ϵ_{11} and S is the shear strain ϵ_{12}. Now the pressure in the solid medium can be expressed by σ_{11} or σ_{12} to calculate the transmission factor for the longitudinal and shear wave respectively. There is however another factor to take into account, which is the pressure. The boundary condition between a liquid and a solid can be expressed as:

$$\frac{1}{\rho^{(1)}}\frac{\partial p^{(1)}}{\partial n} = \frac{1}{\rho^{(2)}}\frac{\partial p^{(2)}}{\partial n} \tag{3.41}$$

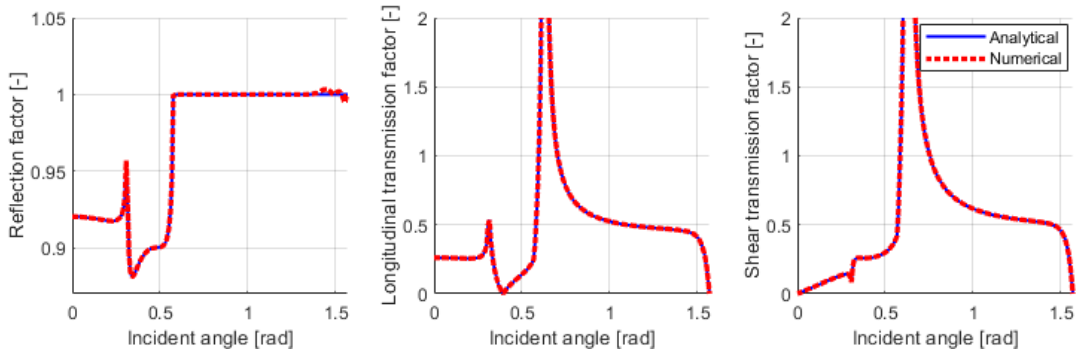

Figure 3.9: Analytical and numerical solution of the reflection and transmission factors as a function of the incident angle for a wave hitting a liquid-solid interface with materials skin and steel (needle) respectively.

Where $\frac{\partial p}{\partial n}$ is the derivative of p along the normal of the interface. The transmission factors TF_L and TF_S are therefore expressed as [6]:

$$TF_{(L/S)} = \frac{\rho^{(1)}}{\rho^{(2)}} \frac{p^{(2)}}{p^{(1)}}. \tag{3.42}$$

Now a comparison between the numerical and analytical results can be made, this is visualised in Fig. 3.9. It can be seen that the analytical and numerical results match for all the reflection and transmission factors. For the reflection factor, there is a peak in the reflection at $\theta = 0.31$ rad, at $\theta = 0.57$ rad the reflection becomes constant and equal to 1. The first peak is at the angle for which the transmitted longitudinal wave becomes parallel to the interface. The moment the reflection factor reaches the constant value of 1, the transmitted shear wave becomes parallel to the interface as well. These events explain the changes taking place in the figure. There is no dependency on the frequency of the wave since the two media are considered to be infinite in length and width.

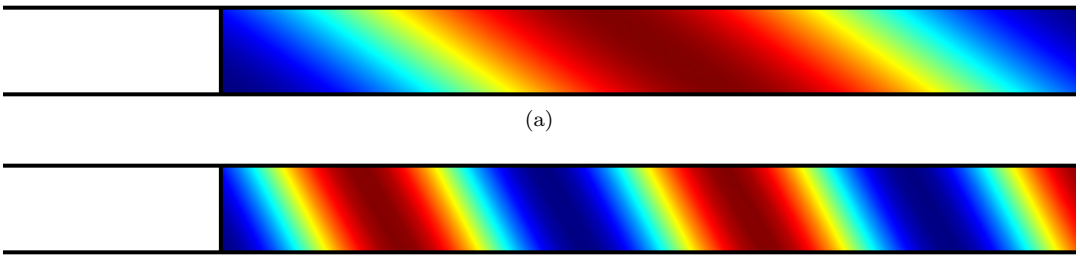

(a)

(b)

Figure 3.10: Resulting waves in the right, solid medium from an incident wave from the left, liquid medium for an incident angle of 0.25 rad. It regards a liquid-solid interface with materials skin and steel (needle) respectively. a) Longitudinal wave in the solid medium. b) Shear wave in the solid medium.

The wave propagation for an incident longitudinal wave with $\theta = 0.25$ rad is visualised in Fig. 3.10. Where 3.10a represents the longitudinal wave propagation in the solid medium and Fig. 3.10b the shear wave propagation in the solid medium, calculated using Eqs. (3.39) and (3.40). The wave propagates from left to right. Only the wave propagation in the solid is visualised. It can be seen that the longitudinal wave propagates with a higher velocity than the shear wave. The propagation angle is larger for the longitudinal wave as well. Both the velocities and the angles of the waves correspond to the analytically calculated values.

3.5 Liquid-Solid-Solid Interface

Now a three layer interface is considered with at least one solid layer. A general analytical relation for the reflection and transmission of a wave in an arbitrary number of solid layers will be derived. This is an extensive derivation and uses similar concepts as for the derivation of the liquid-solid interface, therefore it can be found in App. A.2. This analytical model will be used in the verification of the numerical COMSOL model.

3.5.1 Numerical Model Verification

To get the numerical solutions for this structure, a COMSOL model setup is used which is equivalent to the model used to evaluate the three layer liquid interface sketched in Fig. 3.5. In this sketch the second or third liquid medium is replaced by a solid medium, no additional changes are applied to the model. The length of the middle layer is $d = 50\mu m$. Two different numerical models are evaluated. First, a simplified structure is considered, where the two outer layers are skin (liquid) and the middle layer is a coating (solid). Next, the liquid-solid-solid case of a skin-coating-needle is considered, the intended final structure. This final study will be similar to the case study of the three liquid interface. Therefore, it can also be investigated to what degree the inclusion of the shear waves contributes to the reflection and transmission factors.

3.5.1.1 Skin-Coating-Skin, Simplified Solution

As a simplification, a three layer structure with liquid properties for the two outer layers and solid properties for the layer in between will be considered first. The complete analytical solution derived in App. A.2 will now be simplified for this specific case; a liquid-solid-liquid problem with the same liquid in the first and last medium. Since the last layer is a liquid instead of a solid, layer n does not support shear waves, resulting in $P/TF = 0$, $\omega_{S,n} = 0$ and $c_{S,n} = 0$. Also, since the number of layers is limited $\mathbf{A} = \mathbf{a}$ applies, simplifying the relations notably. With these simplifications, RF and TF become rather simple [5]:

$$RF = \frac{i(M^2 - N^2 + 1)}{2M + i(M^2 - N^2 - 1)}, \tag{3.43}$$

$$TF = \frac{2N}{2M + i(M^2 - N^2 - 1)} \tag{3.44}$$

with:

$$\begin{aligned} N &= \frac{Z_L^{(2)} \cos^2 2\theta_S^{(2)}}{Z^{(1)} \sin P} + \frac{Z_S^{(2)} \sin^2 2\theta_S^{(2)}}{Z^{(1)} \sin Q}, \\ M &= \frac{Z_L^{(2)}}{Z^{(1)}} \cos^2 2\theta_S^{(2)} \cot P + \frac{Z_S^{(2)}}{Z^{(1)}} \sin^2 2\theta_S^{(2)} \cot Q, \\ P &= k_L^{(2)} d \cos\theta_L^{(2)}, \\ Q &= k_S^{(2)} d \cos\theta_S^{(2)}. \end{aligned} \tag{3.45}$$

This solution can be compared to numerical results. The structure is solved over a frequency range for three different incident angles. A skin-coating-skin setup is used, with the material properties as provided in Table 3.1. The comparison of this numerical model and the analytical model is provided in Fig. 3.11. From this figure it can be seen that the numerical and analytical result of the reflection and transmission factors agree for any angle of incident. When the angle of the incident wave is unequal to 0, the factors give a more complicated frequency dependency with additional peaks. These peaks are related to the harmonics of the propagating shear wave in the middle domain.

The dip occurring for the longitudinal wavelength is equal to the previous problems at frequencies at multiples of: $d = \frac{1}{2}\lambda_{L,n} = \frac{\lambda_L}{2\cos\theta} = \frac{c_L}{2f\cos\theta}$. Which means the first dip for the 0 degree

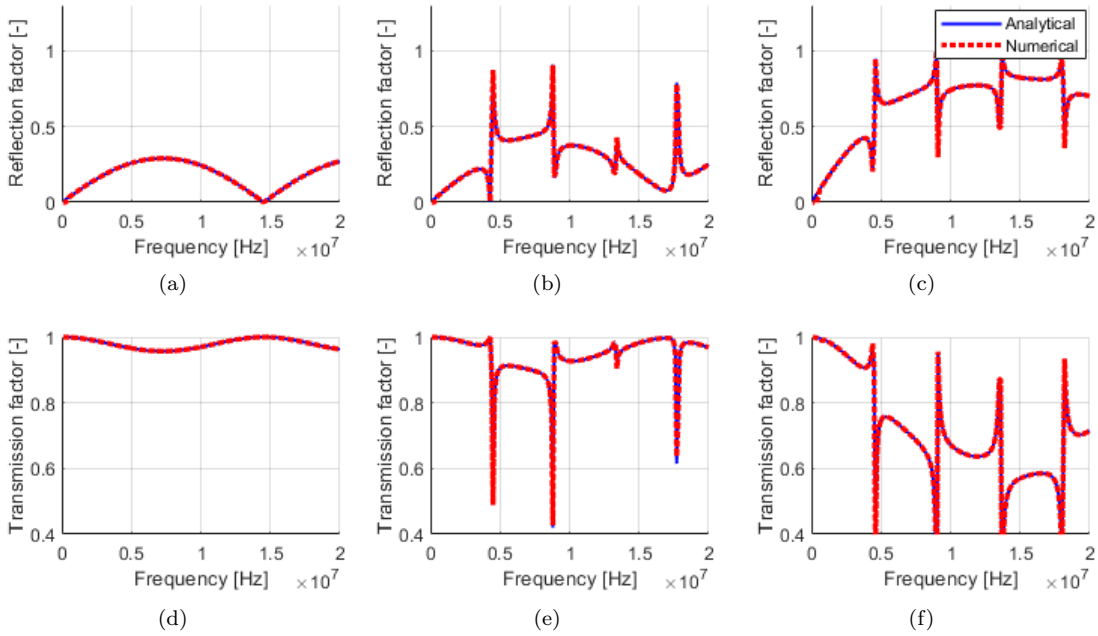

Figure 3.11: Analytical and numerical solution of the reflection and transmission factors as a function of the incident wave frequency for a liquid-solid-liquid interface of skin-coating-skin. (a-c): Reflection factor for a wave with incident angle of 0 rad, $\frac{4}{20}\pi$ rad and $\frac{8}{20}\pi$ rad respectively. (d-f): Transmission factor for a wave with incident angle of 0 rad, $\frac{4}{20}\pi$ rad and $\frac{8}{20}\pi$ rad respectively.

incident angle should be at 14.25 MHz ($d = 50\mu m$), which is in line with the result from Fig. 3.11a. The additional peaks in Figs. 3.11b and 3.11c occur due to the same phenomenon, but now regarding the shear wave. These dips should occur at multiples of: $d = \frac{1}{2}\lambda_{S,n} = \frac{\lambda_S}{2\cos\theta} = \frac{c_S}{2f\cos\theta}$. For the incident wave with angle $\frac{4}{20}\pi$, the first dip will be at a frequency of 4.4 MHz, in agreement with Fig. 3.11b. At multiples of this frequency the higher order harmonics occur.

In Fig. 3.12 the resulting waves from an incident wave with an angle of $\frac{4}{20}\pi$ rad and a frequency of 17.1 MHz are displayed. This is the frequency where the first harmonic of the longitudinal wave occurs. It can be seen that for the longitudinal wave in the solid, Fig. 3.12b, half the wavelength in normal direction to the boundary is equal to the length of the middle layer. The reflected wave has only a small amplitude compared to the transmitted wave, see Fig. 3.12a, which is in agreement with Fig. 3.11. For the shear wave, Fig. 3.12c, is can be seen that almost two wavelengths fit in the middle layer. This is in agreement with the analytically calculated wavelength.

3.5.1.2 Skin-Coating-Needle, Intended Final Structure

For the case where the last layer is considered to be a solid, no assumption can be made in the analytical derivation except for $\mathbf{A} = \mathbf{a}$. In this case, the complete equations leading to Eqs. (A.25), (A.28) and (A.29) have to be solved. For the numerical results from COMSOL, TF is derived using the same method as for the liquid-solid interface problem, Eq. (3.42). The comparison between the analytical and numerical results is given in Fig. 3.13.

From this comparison it can be seen that the analytical and numerical results match. When the reflection factor at a normal angle of incident is examined, this matches the curve for the three liquid interface problem of Fig. 3.6. This is as expected since there will not be a contribution of the shear wave at normal incidence, which should result in a similar curve.

When the incident wave is not normal to the boundaries, numerous peaks arise in the figures for the reflection and transmission factors. These peaks are caused by the shear wave. But now the peaks are not at $\lambda_S = \frac{c_S}{2f}n$ with $\mathbb{Z}_n = 1, ., n$, which was the case for the liquid-solid-liquid

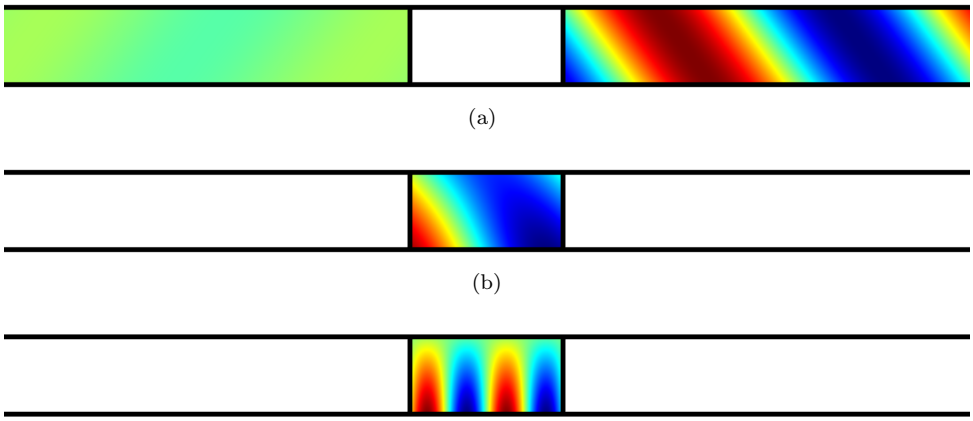

Figure 3.12: Resulting waves from incident wave from left medium for an incident angle of $\frac{4}{20}\pi$ rad and a frequency of 17.1 MHz for skin-coating-skin, liquid-solid-liquid problem. There is a slight reflection and great transmission. a) Longitudinal wave in liquid. b) Longitudinal wave in solid. c) Shear wave in solid.

interface, but at $\lambda_S = \frac{c_S}{2f}(n - \frac{1}{2})$ with $\mathbb{Z}_n = 1, ..., n$. This is because the boundary conditions have changed in comparison to the liquid-solid-liquid problem. Since there is no shear possible in the liquid and the stresses must be continuous, at the liquid-solid interface the shear stress in the solid will be zero as well, see Fig. 3.14. Meaning that the resulting shear waves are caused by the kinematic boundary conditions at the this type of interface. This means that for the liquid-solid-*liquid* problem the shear stresses are zero at both sides of the middle layer resulting in peaks at multiples of half the wave length. But when the liquid-solid-*solid* structure is considered, the stresses will be zero at one side and at a peak at the other side as can be seen in Fig. 3.14. Resulting in a shift of the resonance peaks with $\frac{1}{4}\lambda$. Therefore the peaks of maximum reflection take place at $\frac{1}{4}\lambda_S$, $\frac{3}{4}\lambda_S$, etc..

The resulting waves are visualised in Fig. 3.15. From this figure it can be seen that at a shear wave resonance frequency, exactly $1\frac{3}{4}$ wavelength fits into the middle layer, see Fig. 3.15c.

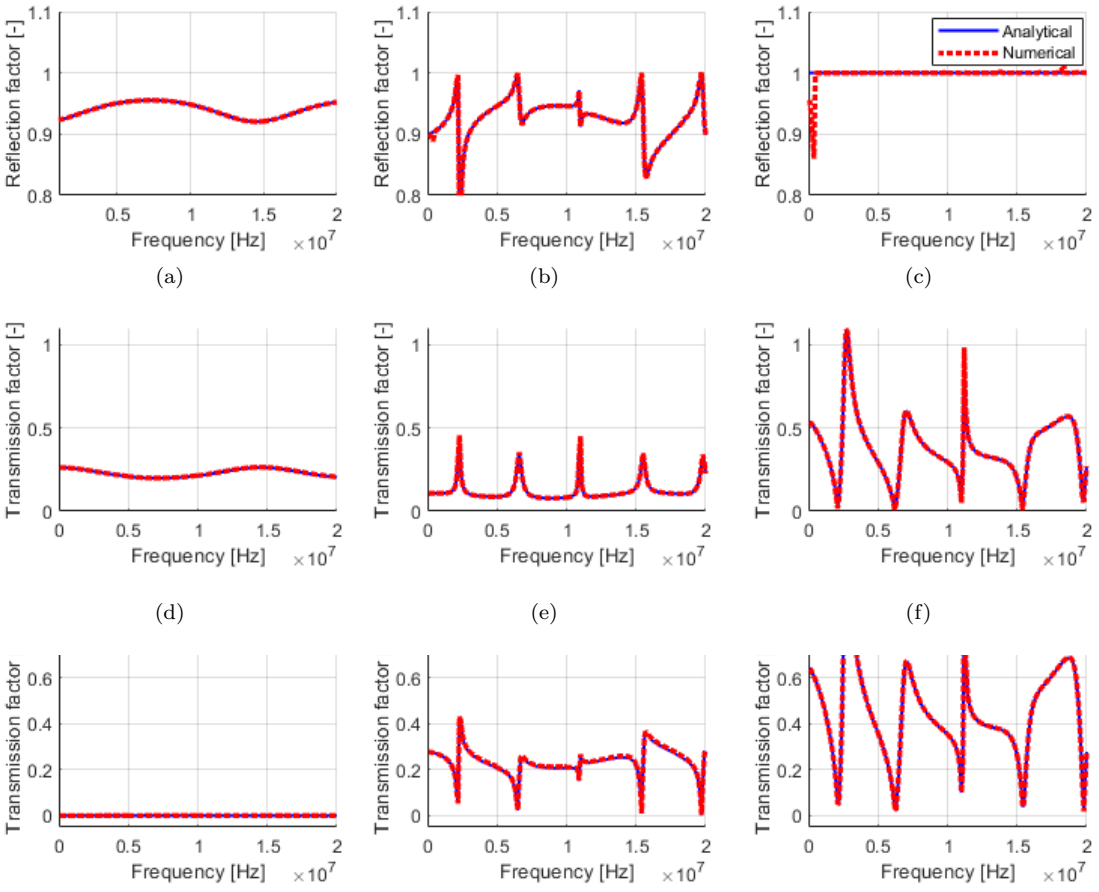

Figure 3.13: Analytical and numerical solution of the reflection and transmission factors as a function of the incident wave frequency for a liquid-solid-solid interface of skin-coating-steel. (a-c): Reflection factor for a wave with incident angle of 0 rad, $\frac{3}{20}\pi$ rad and $\frac{6}{20}\pi$ rad respectively. (d-f): Transmission factor of longitudinal wave for a wave with incident angle of 0 rad, $\frac{3}{20}\pi$ rad and $\frac{6}{20}\pi$ rad respectively. (g-i): Shear wave transmission factor for a wave with incident angle of 0 rad, $\frac{3}{20}\pi$ rad and $\frac{6}{20}\pi$ rad respectively.

Figure 3.14: Shear component of the stress tensor. At the liquid-solid interface, between the first and second medium, the shear stress is zero, at the solid-solid interface the shear stress is at a peak.

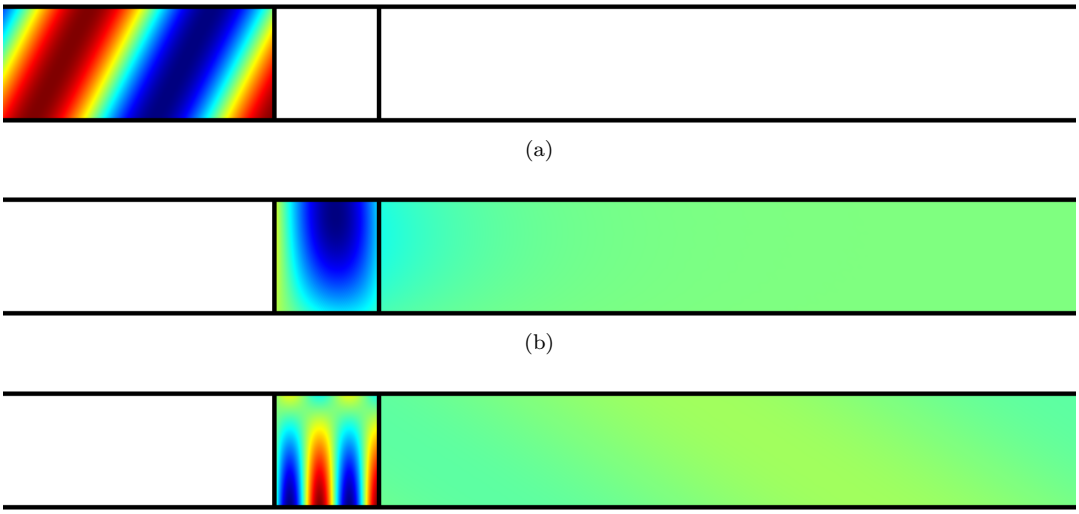

(a)

(b)

(c)

Figure 3.15: Resulting waves from incident wave from left medium for an incident angle of $\frac{3}{20}\pi$ rad and a frequency of 15.5 MHz for skin-coating-steel, liquid-solid-solid problem. a) Longitudinal wave in liquid. b) Longitudinal wave in solid. c) Shear wave in solid.

Chapter 4

Basics on Acoustic Metamaterials

In this chapter, the focus lies on the working principle of acoustic metamaterials. First, different types of acoustic metamaterials are explained and compared. With this information, the focus is directed towards Locally Resonant Acoustic Metamaterials (LRAMs). Lastly, the dynamic behaviour of an one-dimensional LRAM is explained, resulting in a 1D LRAM design.

4.1 Metamaterial Structures

An acoustic metamaterial is a material designed to manipulate waves travelling through this material. The most prominent types of acoustic metamaterials are acoustic gradient metasurface, phononic crystals and locally resonant acoustic metamaterials. The working principle of these types of metamaterials will be explained. When all acoustic metamaterials are examined, a decision is made on which metamaterial to focus on for the remainder of this study.

4.1.1 Acoustic Gradient Metasurface

An acoustic gradient metasurface is designed to redirect an incident wave by steering the reflection back to the source [19]. This acoustic metasurface is structured as labyrinthine units to manipulate the path of the pressure waves. The metasurfaces are designed for a specific frequency since this has an influence on the chamber sizes of the metasurface [20, 21]. An example of such a metasurface can be seen in Fig. 4.1a. The pressure wave will zig-zag through the structure and will have a negative reflection angle on the way back, as can be seen in Fig. 4.1b. A big advantage of this metasurface is this negative reflection since the wave energy needs to be transmitted back to the imaging probe. In practice however, this would not be a feasible needle coating to produce on large scale; the complex structure and the fact that the reflection chambers have to be precisely produced on a micro-scale tend to cause problems.

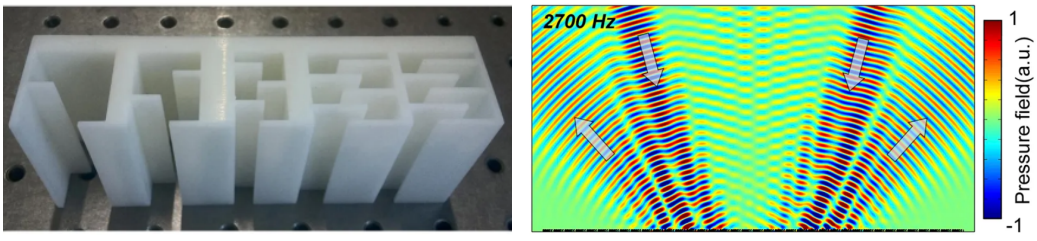

(a) (b)

Figure 4.1: Acoustic gradient metasurface. a) Five different labyrinthine units. b) Broadband frequency response at 2700 Hz, two incident beams at approximately 15 degrees. From Ref. [21].

4.1.2 Phononic Crystal

A Phononic Crystal (PC) is a periodically layered structure that affects the propagation of both longitudinal and shear waves [11]. A PC is designed to stop the propagation of waves with a certain wavelength. When the wavelength of the incident wave matches the length of the PC layers, the reflected wave will be matching this incident wave only with a phase shift of $\pi/2$ rad and a reduced amplitude, see Fig. 4.2a. This will result in a so-called destructive interference with the incident wave, affecting the amplitude of the propagating wave. Since the PC is a periodic structure, the same phenomenon occurs at the subsequent interfaces, ultimately stopping the propagation of the wave in the metamaterial. This simple example of a PC is referred to as an one-dimensional PC, first discovered by Narayanamurti *et al.* in 1979 [27]. The study on two- and three-dimensional PCs did not emerge until the early 1990s, with studies by Sigalas and Economou about structures of a medium with periodically placed cylindrical and spherical inclusions [29, 30]. Since the wavelength must match the layer length, the dimensions of the PC are of the same order as the considered wavelength. Besides, the periodic design limits the attenuation to a single frequency.

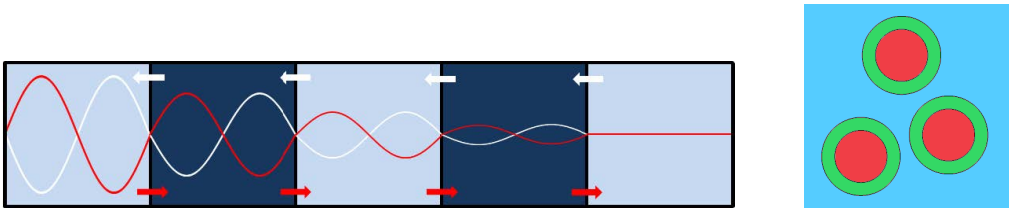

(a) (b)

Figure 4.2: Examples of two types of metamaterials. (a) Phononic crystal (PC); the two colours represent two different materials. The red incident wave is attenuated by a reflected wave of opposite amplitude. (b) Locally resonant acoustic metamaterial (LRAM); heavy core particles coated with a soft rubber material embedded in a matrix material.

4.1.3 Locally Resonant Acoustic Metamaterial (LRAM)

The working principle of a LRAM is different; now the local resonance of inclusions in a matrix material is considered. The inclusions consist of heavy, solid cores coated with a soft material, as can be seen in Fig. 4.2b. The first locally resonant acoustic metamaterial was presented in 2000 by Liu *et al.* [24]. This composite showed band gaps two orders of magnitude smaller than the relevant wavelength [11]. The LRAM particles in this study were lead particles coated with a silicone rubber; making it possible for the lead particle to move independently from the matrix material, subsequently absorbing or amplifying the energy of the incident waves. Since a LRAM resonates locally in the inclusions, periodicity of the inclusions is no longer required. Another property of LRAMs is that they resonate at frequencies two orders of magnitude lower than the relevant wavelength of the LRAM particles, making it possible to produce LRAMs for ultrasound applications.

4.1.4 Metamaterial Type Selection

Since LRAMs do not require a repetitive structure, the production of this metamaterial is significantly easier compared to the other two. Another asset is that the inclusions can easily be produced since they are two orders of magnitude larger than the studied wavelength, this is an important aspect when considering ultrasound applications. Also, the fact that the incoming wave does not require to be in line with the LRAM is an important asset in comparison to PCs. These points show that for the production of a coating for ultrasonic applications, LRAMs are the superior choice. Therefore the focus will be on using LRAMs for the remainder of this study.

4.2 LRAM: Dynamic Behaviour

In this section the dynamic behaviour of a LRAM is explained. The explanation is limited to an one-dimensional problem for simplification.

For a composite structure the effective mass density is given by the volume averaged, homogenised mass density ρ_{hom}. The homogenised mass density ρ_{hom} will only be correct in static fashion. When the structure is excited, the heavy cores will show a relative motion with respect to the matrix material, affecting the effective mass density [26]. When the volume fraction of the inclusions is significant and the combination of the mass with the stiffness of the rubber layer is chosen correctly, this can lead to the appearance of a negative effective mass density [24, 23]. To demonstrate the appearance of a negative mass density, an infinite mass-in-mass lattice structure is considered, as illustrated in Fig. 4.3. Where m_1 represents the mass of the matrix material

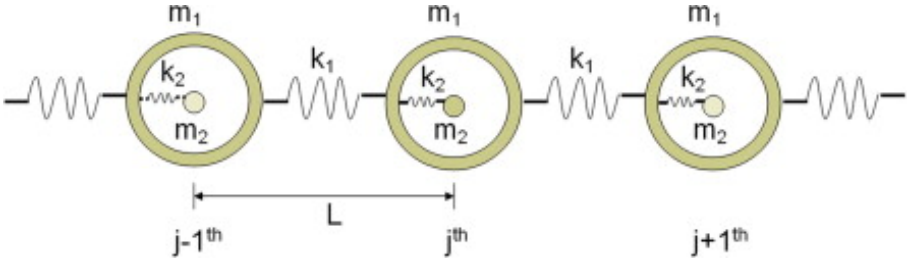

Figure 4.3: An one-dimensional acoustic metamaterial composed of an infinite series of resonators in a lattice structure. From Ref. [14].

and core coating combined, mass m_2 is the mass of the core. The parameters k_1 and k_2 are the stiffness of the matrix material and core coating respectively. An external force F is acting on this structure, resulting in displacements u_1 and u_2 of the matrix material and cores respectively. First, the resonators are considered, excluding the stiffness k_1 between two resonators. When Newton's second law in the frequency domain is applied to this mass-in-mass structure, it can be written as:

$$\sum F = f_2 = (-i\omega)^2 m_2 u_2, \tag{4.1}$$

where the force f_2 can be expressed as a function of the spring parameters using Hooke's law: $f_2 = k_2 (u_1 - u_2)$, resulting in the following equation for the displacement of the core:

$$u_2 = \frac{k_2}{k_2 - \omega^2 m_2} u_1. \tag{4.2}$$

Newton's second law is applied to the complete structure, still excluding k_1, with a dynamic mass density defined as:

$$\rho_{dyn} V = \frac{F}{-\omega^2 u_1}, \qquad \text{with } F = (-i\omega)^2 (m_1 u_1 + m_2 u_2) \tag{4.3}$$

where V is the total volume of the system. By substitution of Eq. (4.2) in Eq. (4.3), a frequency dependent mass density can be derived:

$$\begin{aligned} m_{dyn} = \rho_{dyn} V &= m_1 + m_2 \frac{u_2}{u_1}, \\ &= m_1 + \frac{m_2 k_2}{k_2 - m_2 \omega^2}, \\ &= m_1 + \frac{m_2 \omega_0^2}{\omega_0^2 - \omega^2}, \end{aligned} \tag{4.4}$$

where ω_0 is the resonant frequency of the inclusion defined by: $\omega_0 = \sqrt{k_2/m_2}$.

Now the total structure of j resonators is considered instead of a single one, including stiffness k_1. By doing so, the equation of motion for resonator j can be written as:

$$m_{dyn}\frac{d^2u_j}{dt^2} = k_1(u_{j-1} - 2u_j + u_{j+1}). \tag{4.5}$$

In this equation, u_j can be replaced by an expression of the displacement as a form of propagating waves: $u_j = Ae^{i(kLj+\omega t)}$, where k represents the wavenumber, L the distance between two resonators and A the amplitude of the wave [14]. With this expression for the displacement, Eq. (4.5) can be rewritten as:

$$\omega^2 = -\frac{k_1}{m_{dyn}}\left(e^{\frac{ikL}{2}} - e^{\frac{ikL}{2}}\right)^2, \tag{4.6}$$

and simplified to:

$$\begin{aligned}\omega^2 &= \frac{2k_1(1-\cos kL)}{m_{dyn}},\\ &= \frac{2K(1-\cos kL)}{m_1 + \frac{m_2\omega_0^2}{\omega_0^2-\omega^2}}.\end{aligned} \tag{4.7}$$

With this equation, the band diagram of the structure can be evaluated. The band diagram is a figure where the available frequencies of the structure are plotted as a function of the wave number. A frequency range which cannot be achieved for any wave number is referred to as a band gap. This frequency band diagram is created by solving Eq. (4.7) for different values for k. Also the effective mass density as a function of the frequency can be calculated, used Eq. (4.4). The solution of the effective mass density graph and the corresponding band diagram can be seen in Figs. 4.4a and 4.4b respectively. For this one-dimensional problem, the parameters are adopted from the unit cell described in Sec. 5.1.2.

From Fig. 4.4a it can be seen that for $\omega/\omega_0 \to 0$ the dynamic mass matches the static mass. When $\omega = \omega_0$, the dynamic mass becomes unbounded due to resonance. At frequencies higher than the eigenfrequency the dynamic mass becomes negative. When the frequency surpasses $\omega/\omega_0 = \sqrt{m_{hom}/m_1}$ the dynamic mass becomes positive again. This negative dynamic mass response corresponds to the band gap, visualised as the grey area. Ultimately the frequency becomes too high for the solid inclusion to respond, which results in the dynamic mass asymptotically reaching m_1/m_{hom}. The band gap can be seen again when the band diagram is examined, Fig. 4.4b. The point where $\omega/\omega_0 = 1$ corresponds to the lower bound of the band gap. The turning point where the dynamic mass density becomes positive, corresponds to the higher bound of the band gap: $\omega/\omega_0 = \sqrt{m_{hom}/m_1}$.

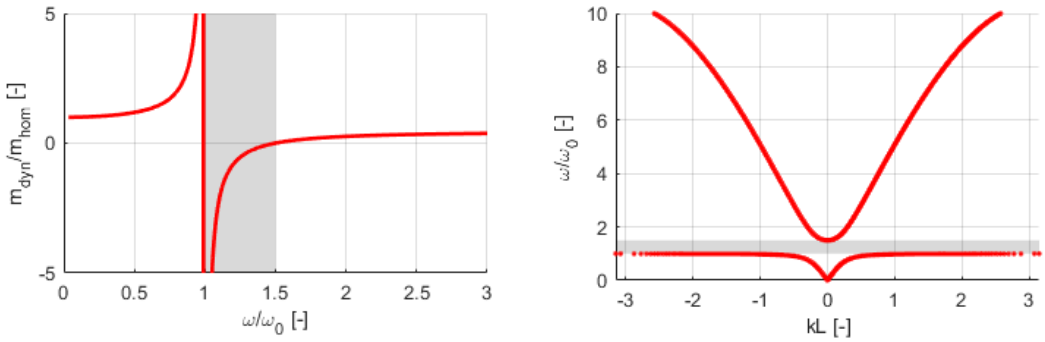

(a) (b)

Figure 4.4: One-dimensional LRAM model with the parameters adopted from the unit cell described in Sec. 5.1.2. The band gap is highlighted as the grey area. a) Effective dimensionless mass as a function of the dimensionless frequency. b) Frequency band diagram.

When a two- or three-dimensional unit cell is considered, the frequency band diagram becomes more complex due to the increasing number of eigenmodes. In the remainder of this study, multi-dimensional unit cells will be considered.

Chapter 5

Metamaterial coating

In this chapter a two-dimensional and three-dimensional needle coating will be designed containing LRAM particles. First, the frequency band diagram of the designed unit cell will be evaluated. Then, the performance of the designed coating will be evaluated, taking into account the dependency on the coating thickness, volume fraction and LRAM particle distribution. The final coating design will be compared to a coating design where the LRAM particles are replaced by voids, which is a different technique to enhance the ultrasound visibility of needles. All evaluations regard a coating with an incident wave normal to the coating boundary. However, the last chapter will evaluate the performance of the metamaterial coating under an angle.

5.1 2D Structure

In this section the performance of a two-dimensional LRAM coating is evaluated. For this evaluation two different models are used. First, the setups of these models are explained. After that, the frequency band diagram of the designed LRAM coating unit cell is evaluated. This band diagram is used to verify whether the skin-coating-needle structure provides logical and accurate results. In this skin-coating-needle structure, the actual reflective performance is evaluated.

5.1.1 Model Setups

As mentioned before, there are two different model setups used to interpret the behaviour of a designed LRAM needle coating. The first setup regards the unit cell of the coating layer, visualised in Fig. 5.1a. For the unit cell designed here, a tungsten core (red) is considered which is covered with a layer of rubber (green). This material combination allows for the tungsten core to resonate in the softer rubber material. These particles are embedded in a polyethylene matrix (blue). The material properties of these materials and the dimensions of the LRAM unit cell can be found in Table 5.1 and 5.2 respectively. The length of the square unit cell L is dependent on the evaluated volume fraction f. The dimensions of the unit cell are selected in such a way that the frequency band gap lies within the desired frequency range for ultrasound guidance (between $2 - 15$ MHz). For the evaluation of the frequency band diagram of this unit cell it is assumed that the structure is infinitely wide and long. Resulting in an infinite primitive square structure, as visualised in Fig. 5.1a. This assumption is supported by applying Floquet-Bloch boundary conditions to the sides of the unit cell. This boundary condition provides preservation of the periodicity of the travelling waves in the medium, while accounting for periodicity of the structure itself as well. For the out of plane direction, plane strain is assumed.

The second model setup is used to evaluate the actual reflection of an incident wave on a coated needle, as visualised in Fig. 5.2. This model consists of three different material domains; skin-coating-needle. An acoustic pressure wave is prescribed in the human tissue layer, mimicking a wave originating from the imaging probe. This probe is assumed to be sufficiently far away to

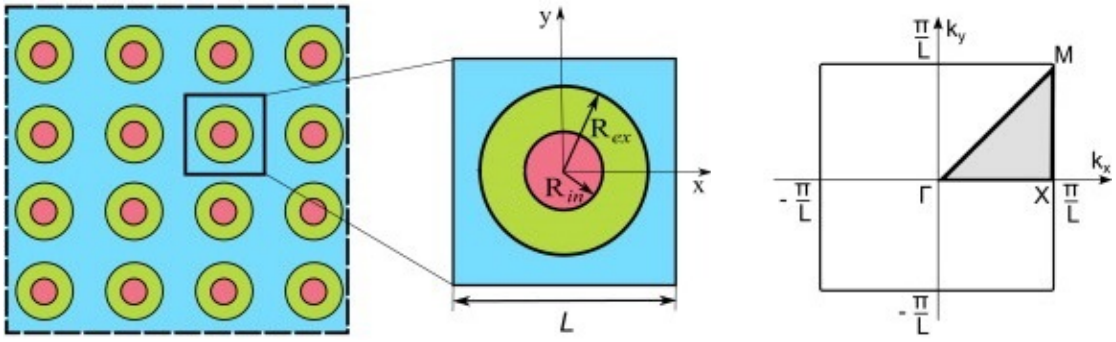

(a) (b)

Figure 5.1: (a) Sketch of a 2D LRAM with a square lattice of inclusions and the corresponding unit cell; (b) the first Brillouin zone (square) and the irreducible Brillouin zone (triangle) for a square lattice. From Ref. [17].

Table 5.1: Material properties used in the analysis of a two-dimensional LRAM unit cell.

Material properties	c_L [m/s]	c_S [m/s]	ρ [kg/m^3]	E [Pa]	ν [–]
Skin [25]	1615	–	1090	–	–
Polyethylene (matrix)	1452	438	900	$0.5 \cdot 10^9$	0.45
Stainless steel (needle)	5302	2976	8000	$180 \cdot 10^9$	0.27
Tungsten (core)	5147	2845	19300	$400 \cdot 10^9$	0.28
Rubber (core coating)	283	55	1100	$0.01 \cdot 10^9$	0.48

Table 5.2: Dimensions of the two-dimensional LRAM unit cell.

Dimensions	Quantity	Unit
R_{in}	$1 \cdot 10^{-6}$	[m]
R_{ex}	$1.5 \cdot 10^{-6}$	[m]
L	$\sqrt{\pi R_{ex}^2 / f} = 4.2 \cdot 10^{-6}$	[m]
f	0.4	[-]

have a plane wave incident on the considered coating domain. For the domain where the wave is travelling through human tissue, the properties of skin are used [25]. Since shear waves hardly propagate in human tissue, this layer is modelled as a liquid. In the coating, the unit cells from the previous model setup are used to form a coating layer. The number of consecutive unit cells can differ and will be indicated with the results. The last layer representing the needle is modelled as stainless steel, which is a conventional needle material.

Different frequencies of the incident wave will be examined to evaluate whether the incident wave will be blocked or be let through by the resonating particles. This is dependent on the band gaps of the unit cell. In the model structure of Fig. 5.2, a couple of assumptions have to be met. The first assumption considers the setup to be infinitely wide, requiring periodic boundary conditions to the sides of the model. To meet this assumption, Floquet-Bloch boundary conditions are applied, equal to the boundary condition explained in the model setup described earlier. Another assumption is that the human tissue layer and steel layer are infinitely long, practically meaning that the energy of all waves travelling away from the structure will disappear. To meet this assumption, at the top and bottom of the COMSOL model a Perfectly Matched Layer (PML) is applied. This layer mathematically dampens the incoming waves without any reflection. Both the boundary conditions can be applied to a liquid medium (human tissue) and solid medium (coating, needle). In the out of plane direction plane strain is assumed. Since the

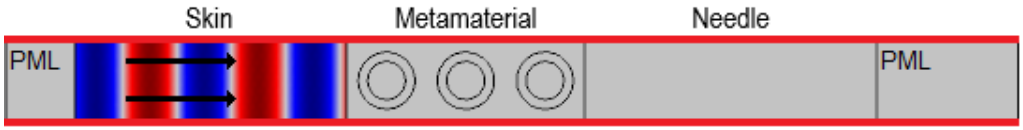

Figure 5.2: Visualisation of the evaluated model setup containing LRAM particles in COMSOL.

perfectly matched layers make the skin and needle domains practically infinitely long, the length of these domains does not affect the performance of the coating. These lengths are therefore variable in the simulations and set at one and a half times the longest wavelength of the medium at the evaluated frequency.

5.1.2 Frequency Band Diagram

Since the unit cells are considered to be structured in a repetitive manner as in Fig. 5.1a, the frequency band structure of the unit cell can be reduced to evaluating the irreducible Brillouin zone (IBZ) due to symmetry. In the previous one-dimensional problem a line evaluation was made over kL. In this two-dimensional case, the evaluation will follow the edge of this triangular IBZ, resulting in the path Γ−X−M−Γ as can be seen in Fig. 5.1b. By evaluating the IBZ, the band structure of the unit cell can calculated, visualised in Fig. 5.3.

From the frequency band diagram of Fig. 5.3 it can be seen that the first band gap is from 4.7 up to 10.5 MHz (highlighted grey area), which is within the ultrasound imaging range. When an incident wave normal to the unit cell is considered, only the $\Gamma - X$ part of the frequency band diagram is considered. For a normal incident wave, a second band gap appears from 20.4 up to 22.5 MHz. For wave frequencies within the band gaps it is impossible for the wave to propagate through the coating. Therefore complete reflection is expected for frequencies lying in the band gap, assuming an infinitely repeated unit cell structure. In the frequency band diagram, the colour distinguishes whether the eigenmode is caused by the propagating longitudinal wave, shear wave or a combination of the two. For a blue colour, at 0, the eigenmode is caused exclusively by a shear wave, when a red colour is observed, at 1, the eigenmode is caused exclusively by the longitudinal wave in the medium. Every colour between 0 and 1 indicates that the eigenmode is generated by a combination of the propagating shear and longitudinal wave. This value is determined by the displacement of the unit cell in the direction of the wave vector in comparison to the total displacement. At the transition around X, from $\Gamma - X$ to $X - M$, a switch in the colours of the eigenmodes can be seen. This is caused by a 90 degree turn of the examined path of the IBZ. A similar situation is seen at the transition from $X - M$ to $X - \Gamma$, the change of colour is less intense due to the 45 degree diversion.

Two other properties of the unit cell which can be derived from the frequency band diagram are the homogenised longitudinal and shear wave velocity. These are by definition related to the slope of the longitudinal and shear waves originating from point (Γ,0). For this unit cell, the homogeneous velocities are calculated to be: $c_L = 245.4$ m/s and $c_S = 90.1$ m/s. These values are used later to make a comparison of the performance of the unit cell structure with its homogeneous equivalent; with the longitudinal velocity, shear velocity and static homogenised mass density, the homogenised material properties can be determined.

To get an idea of the displacements in the unit cell for different eigenmodes, the mode shapes at six different locations in the band diagram are visualised as the displacement of the unit cells. This can be seen in Fig. 5.3, the colouring in these figures show what part of the unit cell is in motion for a particular eigenmode.

For the unit cell with eigenmode of Fig. 5.4a it can be seen that the excitation is rotational symmetric. The maximum excitation is in the core-rubber boundary, indicating a rotation of the core and rubber in the unit cell. Since this rotational excitation does not translate to an excitation of the matrix material, this eigenmode does not have an effect on the reflection and transmission factors. For the eigenmode of Fig. 5.4f, an equal interpretation can be adopted. This

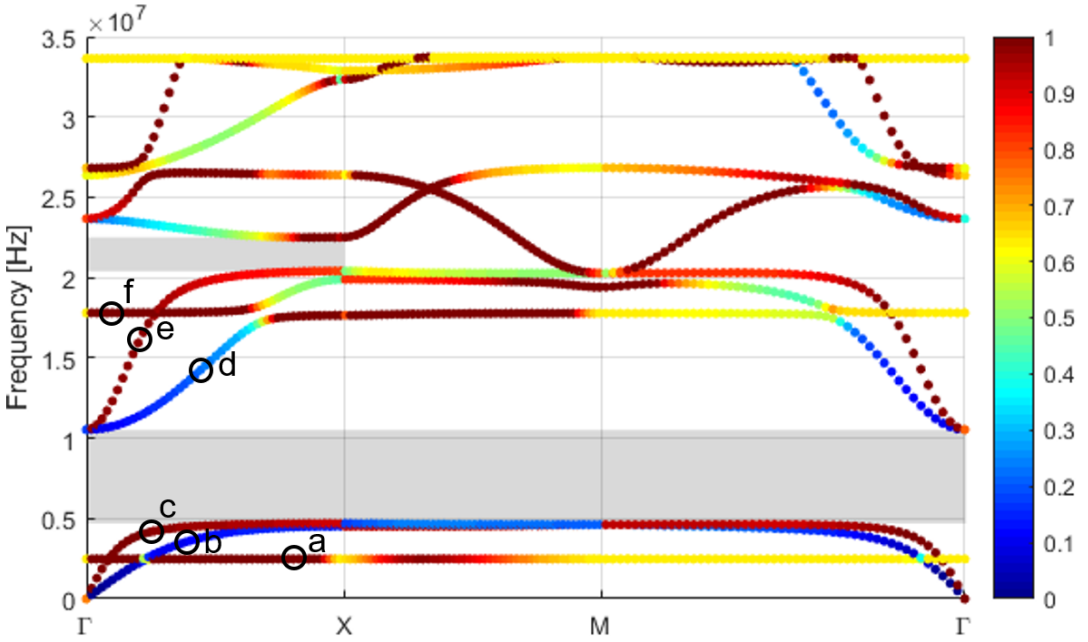

Figure 5.3: Frequency band diagram for the unit cell visualised in Fig. 5.1 with material and unit cell properties from Tables 5.1 and 5.2. The band gaps are highlighted as grey areas. For the colourbar: 0 = purely a shear wave, 1 = purely a longitudinal wave. Colourbar from Ref. [31].

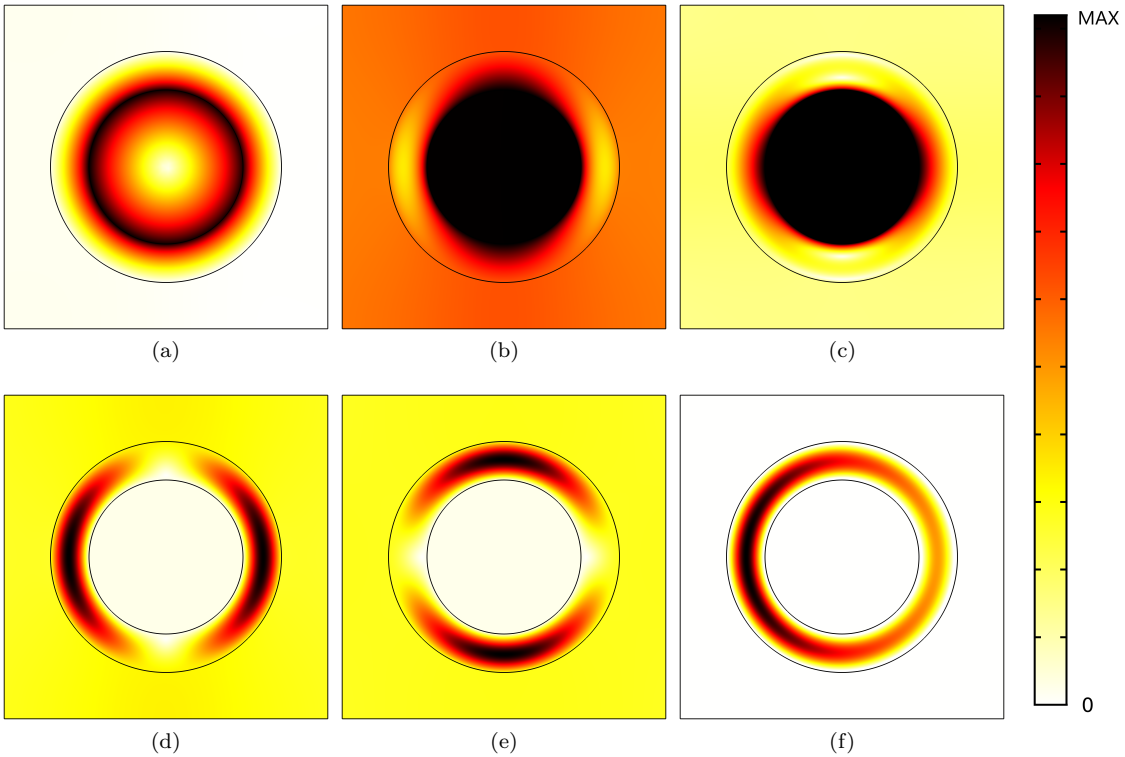

Figure 5.4: Mode shapes of some local resonant eigenmodes. The corresponding position in the frequency band diagram is indicated in Fig. 5.3. The Colours range from no displacement to the maximum displacement, which can be different for every mode shape.

eigenmode is rotational symmetric with the maximum excitation in the rubber layer, an excitation not contributing to manipulation of the travelling longitudinal and shear wave.

The eigenmode of Fig. 5.4b does show a displacement of the matrix material. Therefore this mode does contribute to manipulating incident waves. This excitation is caused by an excitation of the core perpendicular to the examined (horizontal) $\Gamma - X$ direction. Therefore this excitation is caused by the shear wave, this is in agreement with the colour in the frequency band diagram for the considered eigenmode. When the shear eigenfrequency above the band gap is considered, Fig. 5.4d, an equal eigenmode is observed. Except now, the excitation of the rubber layer instead of that of the core is perpendicular to the examined direction. At these modes the displacements in the unit cells is in accordance with the propagating wave. Therefore these modes do not contribute to redirecting the wave to create a band gap. For Figs. 5.4c and 5.4e, the same eigenmode shapes are observed, except for the direction of the excitation. Since the excitation of the core or rubber layer are now parallel to the examined direction, these can be assigned to be caused by the longitudinal wave, which is in agreement with the location on the frequency band diagram.

In Chapter 4.2 the dynamic behaviour of an one-dimensional LRAM was explained. The statements from that chapter also apply to a two-dimensional unit cell. In the band gaps a negative mass will be observed, this is due to the movement of the LRAM components. In the band gap the displacement of the LRAM components will be in anti-phase with respect to the imposed displacement of the matrix material. However, the inclusions will still show resonance, resulting in a large displacement of the inclusions in comparison to the matrix material. The wave energy will be translated to an anti-phase displacement which keeps the wave from propagating. This will be studied in the next section, where the metamaterial will be implemented in a skin-coating-needle structure.

5.1.3 LRAM Layer Performance

In this section the performance of the LRAM layer is evaluated. To do so, the performance of unit cell used previously is examined for different scenarios. First, different numbers of consecutive unit cells are considered. Then the volume fraction dependency is evaluated, as well as whether the square lattice performs equally to a random distribution of the LRAM particles. Next, the performance of the LRAM coating is compared to the performance of a plain polymer coating and to currently available alternative structures in the field for optimising reflection.

5.1.3.1 Evaluation of Different Number of Consecutive Unit Cells

The coating layer is now modelled consisting of the LRAM unit cells, resulting in the setup introduced in Section 5.1.1. First, a two layer problem is considered, where the first layer is the human tissue and the second is the coating. The incident wave is applied perpendicular to the layer interface. Since the frequency band diagram calculated earlier is a representation of an infinite repeatable structure, the band gaps will have a weaker performance when the unit cells are only repeated a couple of times. Different number of consecutive unit cells are evaluated.

The dimensions of the unit cells are fixed for this evaluation. Therefore increasing the number of consecutive unit cells increases the thickness of the LRAM coating. The results from the LRAM coating are compared to the homogenised structure obtained from the frequency band structure. This comparison is made to see what the actual effect is of using a LRAM coating instead of its homogeneous counterpart, the results are shown in Fig. 5.5. For the LRAM coating it can be seen that the reflection is equal to 1 for the start of the first and second band gap. The whole band gap should hold for an infinite repetition of the unit cells. By increasing the number of consecutive unit cells this complete band gap can indeed be approached, even for only a minimal repetition of the unit cells, being seven times. For Fig. 5.5a there is no additional dip between the two band gaps whereas the other structures do show these dips. These dips are related to the frequency where the wave fits the thickness of the LRAM coating layer. Overall it can be concluded that LRAM coating performs much better than its homogeneous counterpart. Especially within the band gaps the LRAM coating performs well.

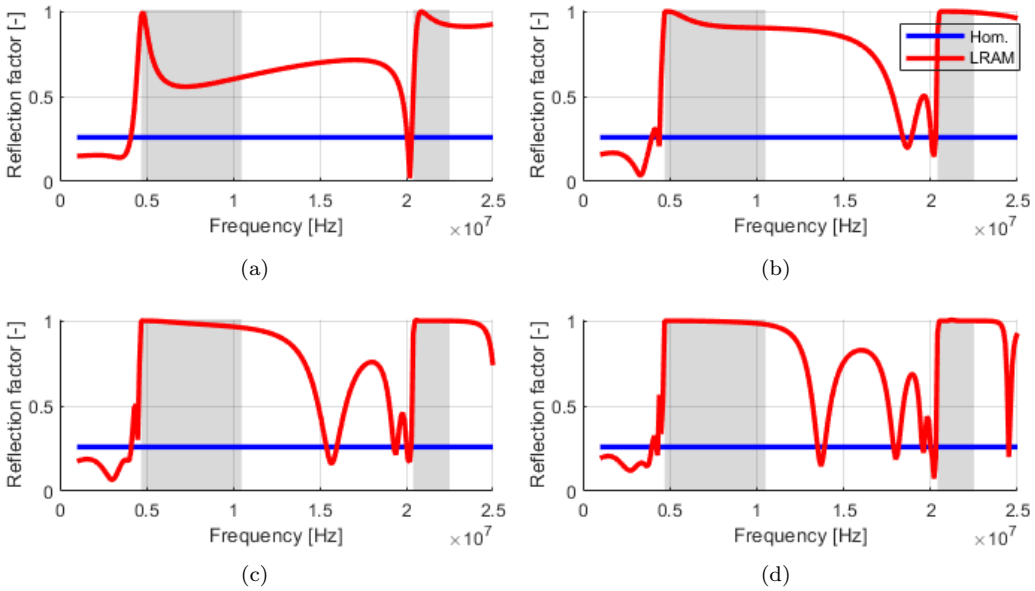

Figure 5.5: Reflection factor for a wave with normal incident on a coating, no reflection possible at the end of the coating layer ($f = 0.4$). Comparison of a LRAM coating and a homogenised coating. For a LRAM consisting of: a) 1 unit cell, b) 3 unit cells, c) 5 unit cells, d) 7 unit cells. The grey areas highlight the band gaps of the unit cell.

The model is now expanded by including the third layer to the structure, the steel needle. This allows for reflection from the interface between the second and third layer. Therefore it is expected that this results in a higher reflection over the complete frequency range. The results from the evaluation of the reflection for this structure are displayed in Fig. 5.6. The dependence on the number of consecutive unit cells is evaluated for this three layer model as well. It can be seen that the reflection of the LRAM is increased over the whole frequency domain as compared to the two layer problem of Fig. 5.5. Within the band gaps, the reflection factor approaches 1. When the number of consecutive unit cells is increased to the point where the first dip should fall within the band gap, the band gap still holds. Meaning the reflection factor will be 1 within the band gaps whatever the amount of repetitions of the unit cells, this is visualised in the figure in App. B.1.

The overall shape of the curve did not change compared to the two layer structure; the peaks and dips are located at the same frequencies. For the application of the LRAM coating it is important to have a reflection of 1 over a wide frequency range, therefore the ultimate structure consists of $3 - 5$ consecutive unit cells.

To get a better understanding of the shape of these reflection factor curves, the vertical stress component (σ_{22}) is visualised at some key frequencies in Fig. 5.7. The frequencies are selected from the coating structure with three consecutive unit cells. Fig. 5.7a, just before the band gap, shows that the metamaterial coating moves in accordance with the propagating wave, as expected from the eigenmodes from Fig. 5.4. Resulting in stress caried through to the needle layer, which translates to a loss of energy travelling back to the human tissue layer. Figs. 5.7b and 5.7c are within the band gap, at 4.8 MHz and 10 MHz respectively. Here, the amount of stress energy propagating through the coating layer is low. For the last figure, Fig. 5.7d, the frequency is chosen exactly in the first dip in the reflection factor. For this case it can be seen that half a wavelength fits into the metamaterial coating layer. This is the first harmonic, as explained in Chapter 3.3.2.1. This also allows for energy to propagate through the metamaterial coating layer, resulting in a dip in the reflection factor.

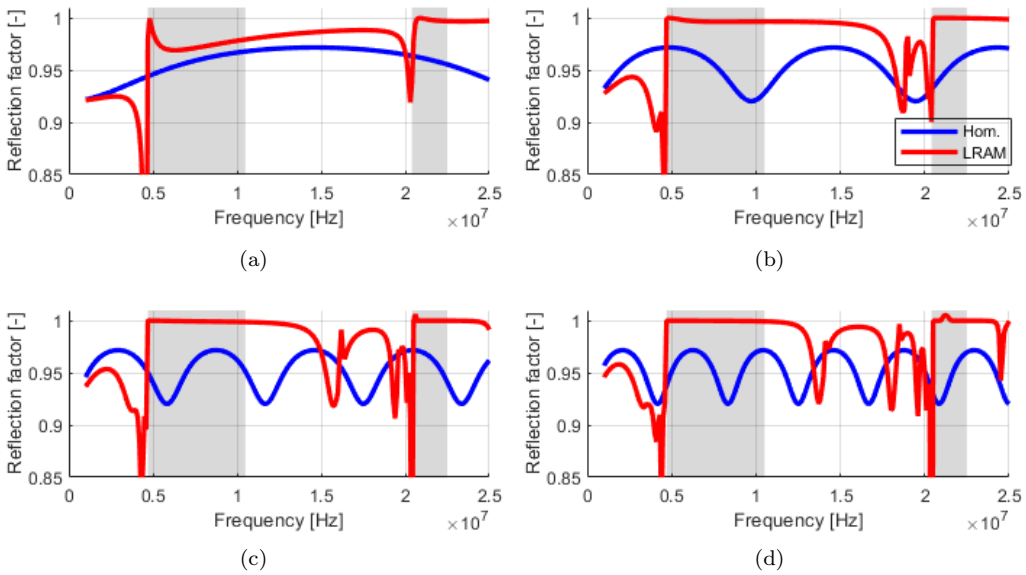

Figure 5.6: Reflection factor for a wave with normal incident on a coating ($f = 0.4$), skin-coating-steel structure. Comparison of a LRAM coating and a homogenised coating. For a LRAM consisting of: a) 1 unit cell, b) 3 consecutive unit cells, c) 5 consecutive unit cells, d) 7 consecutive unit cells. The grey areas highlight the band gaps of the unit cell.

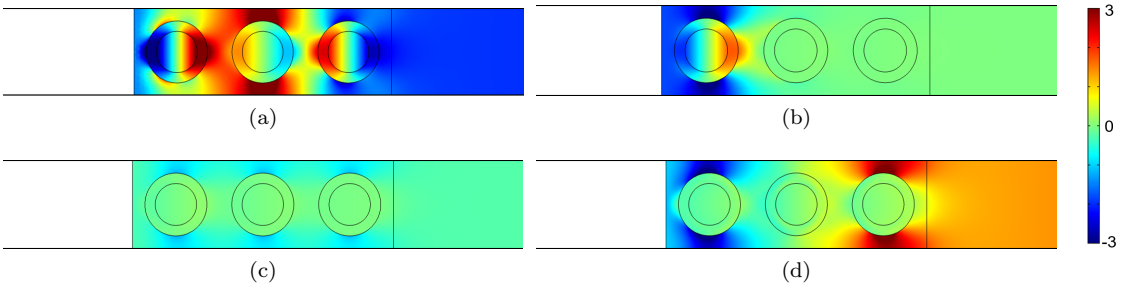

Figure 5.7: Normalised horizontal stress component in the coating layer with three unit cells ($f = 0.4$). a) At 4.6 MHz. b) At 4.8 MHz. c) At 10 MHz. d) At 18.7 MHz.

5.1.3.2 Evaluation of LRAM Particle Volume Fraction

To examine to what extend the reflection factor is related to the volume fraction of the LRAM particles in the coating, the basic metamaterial coating with five consecutive unit cells is evaluated for different volume fractions. The sizes of the tungsten cores and rubber coatings are unchanged in the course of this evaluation, the length of the square unit cell L is dependent on the volume fraction f to adapt for the volume fraction. The volume fraction is defined as the volume of the rubber coating and tungsten core with respect to the total unit cell volume. The results of this evaluation are visualised in Fig. 5.8. From this figure it shows that a higher volume fraction results in a wider band gap. While preserving a similar shape of the curve, at volume fraction $f = 0.2$ the reflection factor decreases right after the start of the band gap. Whereas for a volume fraction of $f = 0.4$ and $f = 0.6$ there is some sort of plateau region with reflection factor close to 1. This difference is due to the spread of the incident wave energy; when the particles in the metamaterial coating are large compared to the lattice constant, the wave wave energy will move to these particles easier (high volume fraction). For a low volume fraction the incident wave will be able to pass the unit cells with less effort, resulting in more energy propagating through the

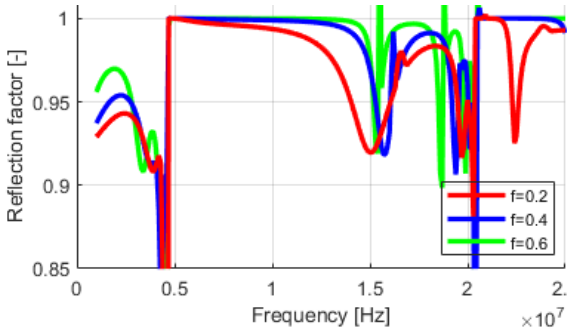

Figure 5.8: Evaluation of the influence of LRAM particle volume fraction, f, in the matrix. For a structure with five consecutive unit cells.

metamaterial coating layer. This region with reflection factor 1 is important since a maximum reflection over a frequency range is desired, therefore the minimum volume fraction must preferably be at least $f = 0.4$. In addition, there is no necessity to increase the volume fraction even further since this does not effect the reflection factor significantly. Another observation from Fig. 5.8 is the first dip is at different frequencies. This dip is caused by the first harmonic which is related to the metamaterial layer length and the wave propagation velocity. The different volume fractions resulted in different lattice lengths ($L = \sqrt{\pi R_{ex}^2/f}$), therefore the metamaterial lengths are not equal. The propagation velocities will be different as well due to the different size of the unit cells. Ultimately, this results in different frequencies for the first dip to occur.

5.1.3.3 Evaluation of LRAM Particle Distribution

Another factor that might influence the reflection is the distribution of LRAM particles in the matrix. For practical applications of the LRAM coating this would be desirable since a coating of randomly distributed particles is easier to manufacture. In Fig. 5.9c, a coating with particles in a square lattice is compared to its random equivalents. The comparison is executed for a structure with a metamaterial domain of five unit cells in length and three unit cells in width, the volume fraction is $f = 0.4$. Fifteen particles are randomly distributed in this domain to get an evaluation with exactly the same volume fraction. The comparison is made to two different random distributions, to make sure to have good representations of random distributions. From these random distributions the particle positions are visualised in Figs. 5.9a and 5.9b. For the randomly distributed LRAM particles it can be seen that the number of dips has increased. The irregular distribution of the particles results in a different distribution of the stresses throughout the metamaterial layer. This will result in local stress concentrations. These concentrations allow for the shear wave to be triggered, even when the incident wave is normal to the coating interface. The dip in the random particle distributions at 12.4 MHz is at the first harmonic of the shear wave. These dips for the shear wave will however not influence the reflection within the band gap, in this frequency region no additional dips occur. Only at frequencies outside the band gap the random distributions get more peaks, which means the band gap of the evaluated unit cells is preserved.

5.1.3.4 Comparison: LRAM to Alternatives

In this section the performance of the LRAM coating will be compared to an alternative needle coating used for EUS-FNA. But first, the improvement in reflection will be evaluated with respect to a plain needle and a needle with a plain polymer coating, see Fig. 5.10. The comparison is carried out for coatings with three and five consecutive unit cells with volume fraction $f = 0.4$. The incident wave is normal to the interface. The polymer coating has the same dimensions as the metamaterial coating and is a homogeneous coating with the material properties of the matrix

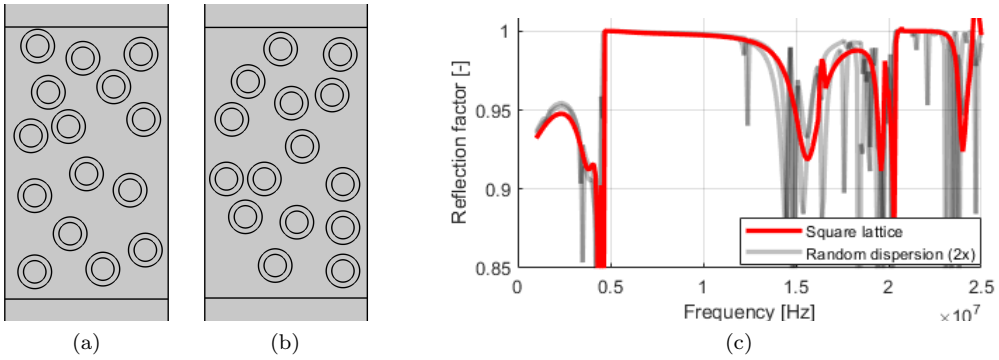

(a) (b) (c)

Figure 5.9: Evaluation of the influence of LRAM particle distribution in the matrix. a,b) Random distributions. c) Reflection factor of a square lattice distribution compared to two random distributions with five consecutive unit cells and ($f = 0.4$).

material of the metamaterial. The results for no coating are from an incident layer directly on the steel layer; the coating layer is removed completely.

In this comparison it can be seen that the reflection factor for an untreated needle is already at 0.92. When the plain polymer coating is considered, only a small improvement of the reflection factor is observed. The increasing reflection factor for an increasing frequency is related to the harmonics of the wave in the polymer domain. The LRAM coating is performing much better, especially for frequencies in the band gap of the unit cell. For low frequencies, the reflection factors of all three structures meet at the reflection factor of the skin-steel structure. This is because for low frequencies the inclusions will not respond to the propagating wave; the reflection will be related to the largest impedance mismatch between the layers. Since this is between skin and steel media, all three structures have equal static reflection factors. Overall, it can be concluded that the LRAM coating performs better within its designed frequency range.

Now, the LRAM coating is compared to an alternative needle for EUS-FNA applications: a polymer coating with voids. For the material coating with voids the LRAM unit cell is changed; the tungsten core particle is replaced by a void and the domain belonging to the rubber core coating is added to the matrix domain. Resulting in the matrix material containing voids with radius R_{in}. The voids are modelled as a vacuum; no material is assigned to the void domains.

In Fig. 5.11 this comparison is executed for three and five consecutive unit cells in the coating. The results show that the void structure gives a good response for a certain frequency range. This region of a good response is however highly dependent on the height of the coating layer. By the

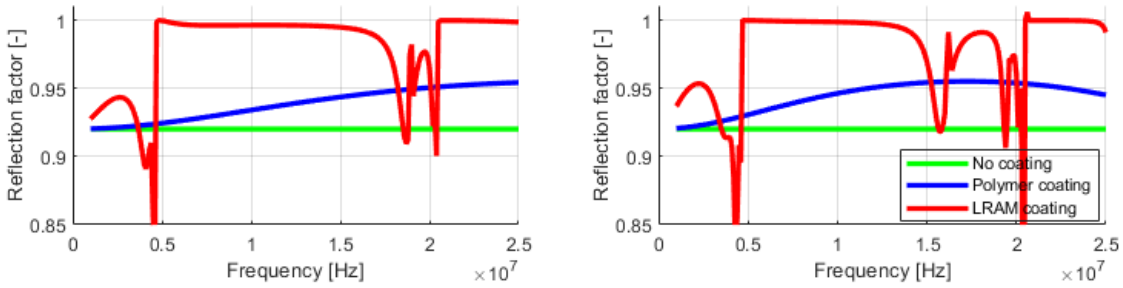

Figure 5.10: Reflection factor for a normal incident wave for a needle without any coating, a plain polymer coating and a LRAM coating. The height of the plain polymer coating matches the height of the evaluated LRAM structure ($f = 0.4$). a) Three consecutive unit cells. b) Five consecutive unit cells.

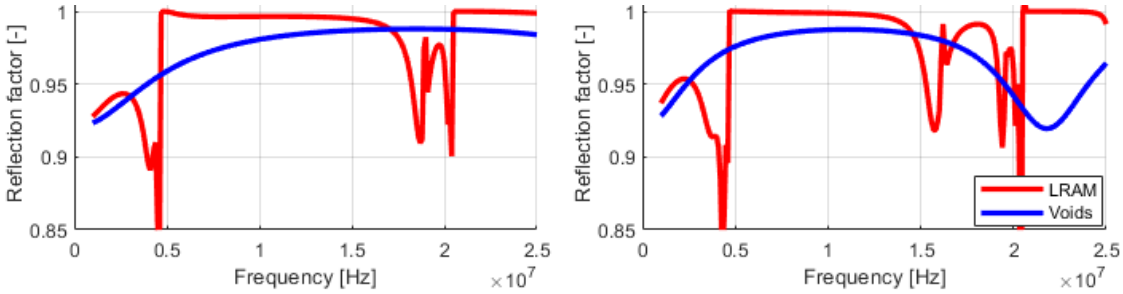

Figure 5.11: Reflection factor for a normal incident wave for the LRAM coating compared to a commercially available coating structure; a coating with voids ($f = 0.4$). The length of the metamaterial and void coating match. a) Three consecutive unit cells. b) Five consecutive unit cells.

shape of the curves it can be seen that the first dip is again dependent on the wavelength fitting in the coating layer, equal to Fig. 5.7d. Therefore the frequency which gives a high reflection is unreliable. For example, the reflection for a coating domain of three consecutive unit cells (Fig. 5.11a) gives a good reflection at 22 MHz, whereas this frequency for the five consecutive unit cells is at the dip for the reflection factor. For the metamaterial coating the thickness of the coating does not play a role for the location of the maximum reflection. Overall, it is more difficult to design a polymer coating with voids to perform well for a specific frequency range. In addition, the polymer coating does not reach a complete reflection (reflection factor of 1), whereas the LRAM has complete reflection at a frequency range it is designed for. This 1.5% difference does not look like a big improvement, but since an ordinary needle already has a 92% reflection and is often poorly visible, this is a huge improvement.

5.2 3D Structure

For the evaluation of the three-dimensional structure an equal approach is used as for the two-dimensional case. First, the model setup is explained. Next, the band diagram will be evaluated to locate the band gap. Then, the reflection factor will be evaluated for a different number of consecutive unit cells and for different volume fractions. Lastly, the performance of the 3D metamaterial structure will be compared to the alternative coating containing voids.

5.2.1 Model Setup

For the three dimensional case, exactly the same model setup is used as for the two dimensional case discussed earlier. The only difference is that the cores are modelled as spheres, as can be seen from the unit cell visualised in Fig. 5.12. The dimensions and materials of this structure are equal to the 2D structure and can be found in Tables 5.1 and 5.2. Except for the calculation of the lattice length L. To get the right three-dimensional volume fraction corresponding to f, the lattice length is calculated as: $\left(\frac{4}{3}\pi R_{ex}^3/f\right)^{1/3}$. The metamaterial unit cell is assumed to be infinitely long in all directions, therefore Floquet-Bloch conditions are applied to all sides of the unit cell cube. The frequency band diagram is displayed for a volume fraction of $f = 0.2$.

The model used for the evaluation of the reflection factor is similar as well, including the boundary conditions: the sides are constrained with Floquet-Bloch boundary conditions, whereas the infinitely long top and bottom of the model are constrained by perfectly matched layers; making incident waves to mathematically dampen out, not allowing for any reflection of the wave.

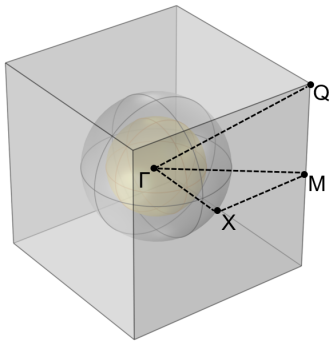

Figure 5.12: Three dimensional unit cell used in the 3D structure evaluation. Paths of irreducible Brillouin zone are highlighted by the dashed lines.

5.2.2 Frequency Band Diagram

To locate the band gaps of the three-dimensional unit cell, the frequency band diagram is examined. Due to symmetry of the unit cell, the evaluation of the frequency band diagram can be reduced to the IBZ, spanned by Γ−X−M−Γ−Q for the 3D unit cell of Fig. 5.12.

The frequency band diagram for the 3D unit cell is visualised in Fig. 5.13, the meaning of the colouring of the points on the diagram is equal to that of Fig. 5.3; indicating whether an eigenfrequency is caused by a longitudinal or shear wave (0 = pure shear wave, 1 = pure longitudinal wave). This value is determined by the displacement of the unit cell in the direction of the wave vector in comparison to the total displacement. The frequency band evaluation is performed for frequencies around the first band gap. It can be seen that the structure of the band diagram is closely related to the 2D band diagram. The start of the band gap is located at the same frequency as for the two-dimensional unit cell, at 4.7 MHz. An important difference with the 2D case however is the size of the band gap. The 3D unit cell has a band gap of only 2.4 MHz (4.7 − 7.1 MHz), whereas the 2D bandwidth was 5.8 MHz. Of course, this is largely related to the evaluated volume fraction of the unit cell, but it has to be noted that it is more difficult to achieve high volume fractions for 3D structures.

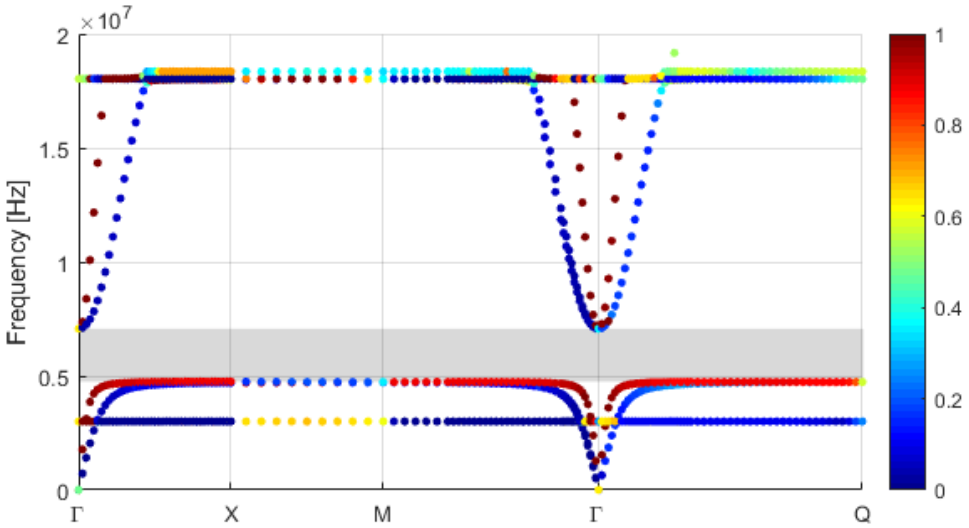

Figure 5.13: Frequency band diagram for the 3D unit cell visualised in Fig. 5.12 with volume fraction $f = 0.4$. The band gap is highlighted as the grey area. For the colour bar: 0 = purely a shear wave, 1 = purely a longitudinal wave. Colourbar from Ref. [31].

5.2.3 LRAM Performance

Just as for the two-dimensional case, the performance of the 3D unit cell is evaluated as a coating. First, coatings with a different number of consecutive unit cells are concerned. The reflection factors for 3, 5 and 7 consecutive unit cells are compared in Fig. 5.14a, with a volume fraction of $f = 0.2$. For the two-dimensional unit cell evaluation only three consecutive unit cells was sufficient. For the three dimensional unit cell more repetitions are required to reduce the dip just after the start of the band gap: the coating should preferably consist of at least seven consecutive unit cells to minimise this effect. However, the first dip of this coating is within the $2 - 15$ MHz range. Therefore it is recommended to have a coating height of maximum 5 unit cells, equal to the 2D structure. To evaluate whether it is possible to overcome this dip, different volume fractions are examined.

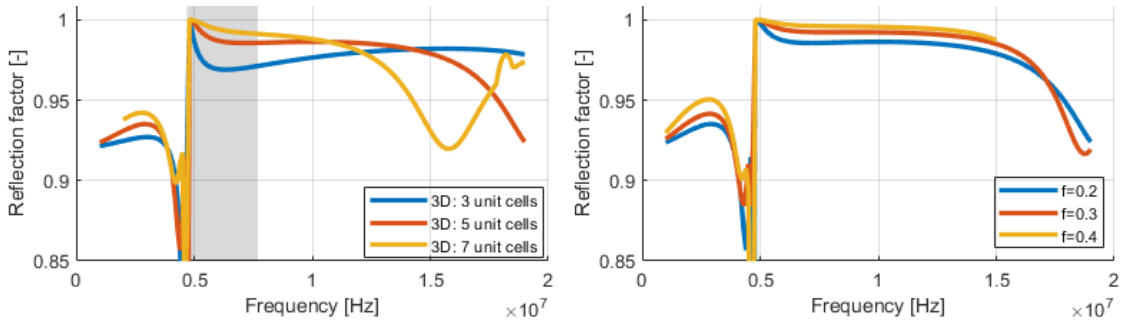

(a) (b)

Figure 5.14: a) Reflection factor for a wave with normal incident on a coating, 3D skin-coating-steel structure. For a LRAM consisting of 3, 5 and 7 consecutive unit cells. The grey area highlights the band gap of the unit cell. b) Evaluation of the influence of LRAM volume fraction, f, for and normal incident wave on a 3D structure with five consecutive unit cells.

The evaluation for different volume fractions is executed for a coating with five consecutive unit cells and is visualised in Fig. 5.14b. A similar trend is observed as for the two-dimensional case: an increasing volume fraction improves the reflection both in and outside the band gap. The dip just after the start of the band gap is reduced as well. Unfortunately, there is no frequency range with a complete reflection. However, the plateau region is at a reflection of more than 0.99. It will be evaluated whether this is a sufficient enough improvement with respect to the performance of a coating with voids.

Lastly, the performance of the 3D metamaterial coating is compared to the performance of a coating with voids. The coating with voids consists of the matrix material, the voids are the same size as the core particles in the metamaterial coating. It can be seen that the reflection of the LRAM coating is considerably higher than that of the coating with voids. Just as for the two-dimensional case, the coating containing voids is dependent on the thickness.

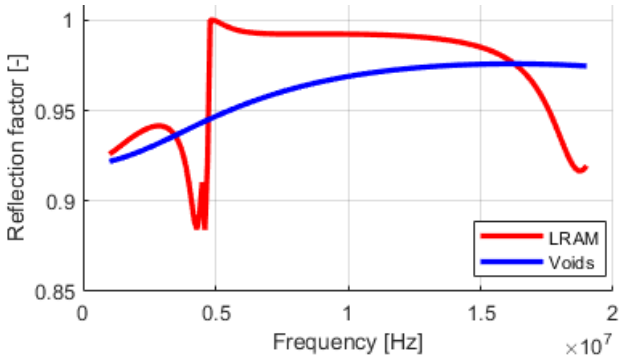

Figure 5.15: Comparison of the LRAM coating with a commercially available coating structure; a coating with voids. Five consecutive unit cells, $f = 0.3$.

5.3 Wave Angle Evaluation

Up to now the performance of the LRAM coating is evaluated for incident waves normal to the surface, a zero degree angle. During ultrasound needle guidance, the incident angle on the needle surface is typically between 40 and 60 degrees, therefore it is important to evaluate the performance of the designed metamaterial under an angle as well. These evaluations will be executed by using the same structure as for the 2D LRAM coating performance structure of Fig. 5.2, except now five consecutive unit cells are assumed with volume fraction $f = 0.4$. The angle between the propagating direction of this wave and the normal to the boundary is defined as the wave angle. The reflection factor is calculated as a function of the incident wave frequency for the different incident angles, see Fig. 5.16.

In the figure, the reflection coefficient is calculated for an rotated incident wave of respectively 10, 20, 30 and 40 degrees. The same band gaps as for the normal incident angles are used. It must

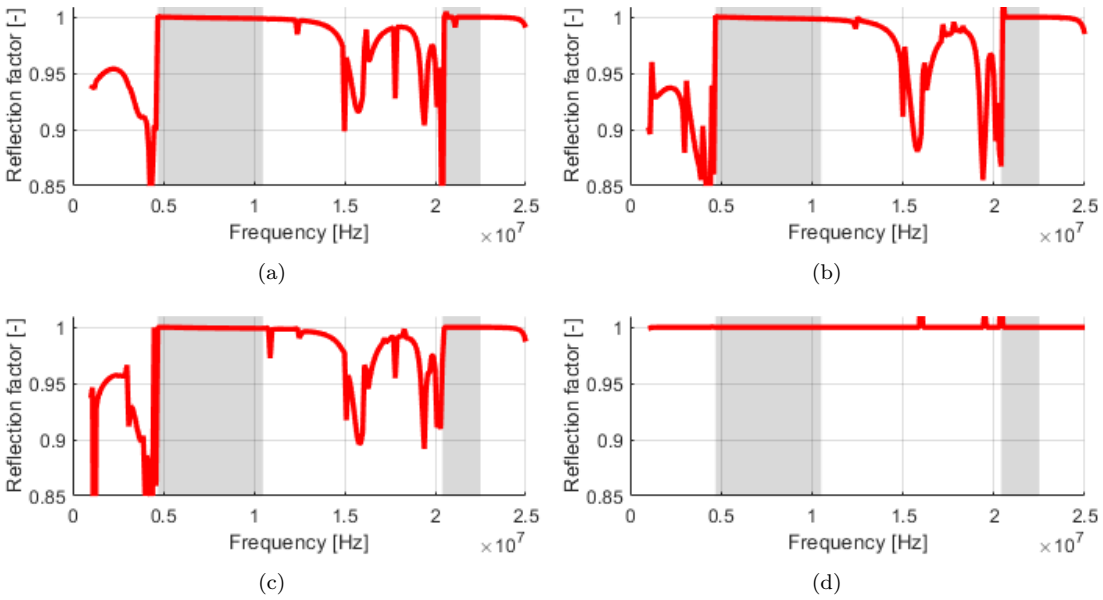

Figure 5.16: Reflection factor for a rotated incident wave on a skin-coating-steel structure with 5 consecutive unit cells. Rotated incident wave: a) 10 degrees, b) 20 degrees, c) 30 degrees, d) 40 degrees. The grey areas highlight the band gaps of the unrotated unit cell.

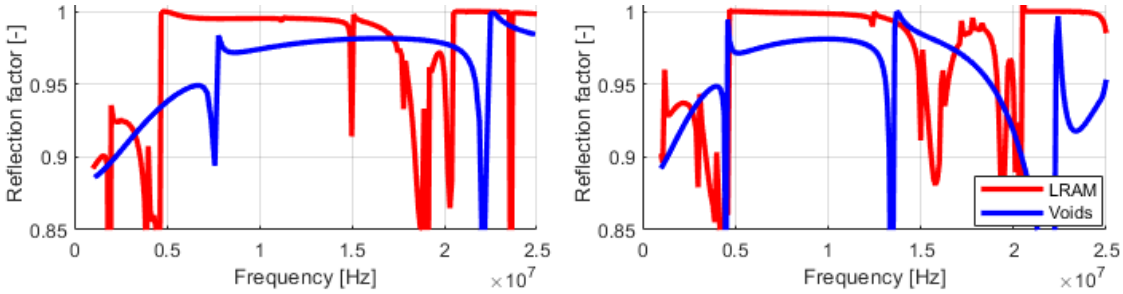

Figure 5.17: Reflection factor for a 20 degree rotated incident wave for the LRAM coating compared to a commercially available coating structure; a coating with voids ($f = 0.4$). The length of the metamaterial and void coating matches. a) Three consecutive unit cells. b) Five consecutive unit cells.

be noted that the band diagram of the 2D unit cell in Fig. 5.3 is not a proper representation of any of the figures displayed here. There is no exact representation since the band diagram show the results for the path $\Gamma-X-M-\Gamma$; the bands for a normal incident wave and a wave under 45 degrees are depicted. Since these two curves show equal band structures, it can be assumed that the wave angles bounded by these two angles show equal results as well.

The results of the reflection factor from Figs. 5.16a-5.16c show similar curves. The evaluation of the unit cell under an angle does not change the frequency regime which shows a complete reflection of the incident wave. It can therefore be concluded that the LRAM functions also for rotated incident waves. There are however some disturbances in the curve which were not present in the evaluations of the normal incident pressure wave of the previous sections. For instance at 12.4 MHz, this small dip is related to the wavelength of the propagating shear wave. Here, exactly a multiple of the wavelength fits into the metamaterial layer. A substantial amount of the shear wave propagating in the metamaterial will be propagating through to the needle, resulting in a loss in wave energy and a dip in the reflection. However, just as for the results with plain layers, Fig. 3.6, there is a limitation to the rotation of the incident angle. This limitation is related to the angular rotation for which Snell's law meets the 90 degrees angle for the target medium. This means a complete reflection of the incident wave.

In Fig. 5.17 the results for the metamaterial coating are compared to the results for the alternative needle coating with voids. Here, the same structures are used as in the comparison between the metamaterial and voids for a normal incident angle, Chapter. 5.1.3.4. The reflection factors are evaluated for a 20 degree incident angle. First of all it can be seen that also the coating structure with voids shows more dips in the reflection factor. These dips are caused by the same phenomenon as for the metamaterial coating: when the angle of incident is rotated a shear wave is created, the harmonics from this additional wave result in additional dips in the reflection. The coating structure with voids performs worse than the metamaterial coating. Since both coatings show similar behaviour for a rotated incident wave, the conclusion formulated for the comparison with a normal incident wave will stand: the metamaterial coating is superior to a polymer coating containing voids.

To see what the reflection for the metamaterial coating actually looks like, the incident and reflected wave for two situations are are displayed. This is chosen at a frequency of 5 MHz, which is within the first band gap and for a rotated incident angle of 20 and 40 degrees. From the figures it can be concluded that the incident and resulting wave are at an equal angle. Meaning that the incident wave has a 'mirror-like' reflection with this kind of unit cell.

Now we go back to the original objective of this project, which is to improve the visibility of medical devices in ultrasound imaging. This 'mirror-like' reflection might therefore not deliver the right performance; when the imaging probe is reasonably far away from the target medical

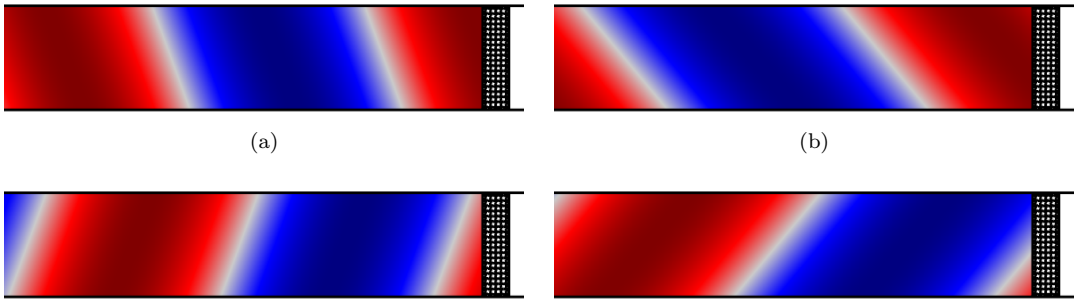

(a) (b)

(c) (d)

Figure 5.18: Pressure wave in the skin medium. a,b) incident pressure wave with an incident angle of 20 and 40 degrees respectively. Wave travelling to the right hand side, incident on the metamaterial coating layer. c,d) reflected pressure wave from the incident angle of 20 and 40 degrees respectively.

device, the reflected wave might not reach this probe. Therefore the reflection angle needs to be manipulated as well. Some new kind of structure that might help with that is a so called LRAM with Double Negativity. This will be elaborated on in the next chapter.

Chapter 6

Double Negative LRAM

The metamaterial design up until now focused on manipulating the incident pressure wave in such a way to achieve an optimal reflection for a certain frequency range. A disadvantage with these structures regarding the original objective is that a wave with a certain incident angle will experience an equal reflection angle. Which means the incident wave will not be reflected back in the direction of the source. In this chapter, a different kind of metamaterial is considered. The main objective of this metamaterial is to manipulate the angle of reflection to propagate back to the source. First, the working principles of such a candidate metamaterial are explained by means of a unit cell design and its performance. Subsequently, the actual performance of this metamaterial will be evaluated by implementing unit cells in the coating layer.

6.1 Double Negative Unit Cell Design

The pursuit for a negative reflecting structure commences by exploring the novel phenomenon of a negative refracting structure. In the last decade several unit cell designs were introduced which were able to capture a frequency range where an incident longitudinal wave exhibits a negative refraction upon propagation through these unit cells [18, 22, 32, 37]. These unit cells have one thing in common: for a negative refraction to occur the effective mass density and effective stiffness both have to be negative, hence the term double negative metamaterial. The double negative unit cell design by Sridhar *et al.* [32] is visualised in Fig. 6.1a. Fig. 6.1b shows an equivalent structure adapted for two dimensional analysis in COMSOL.

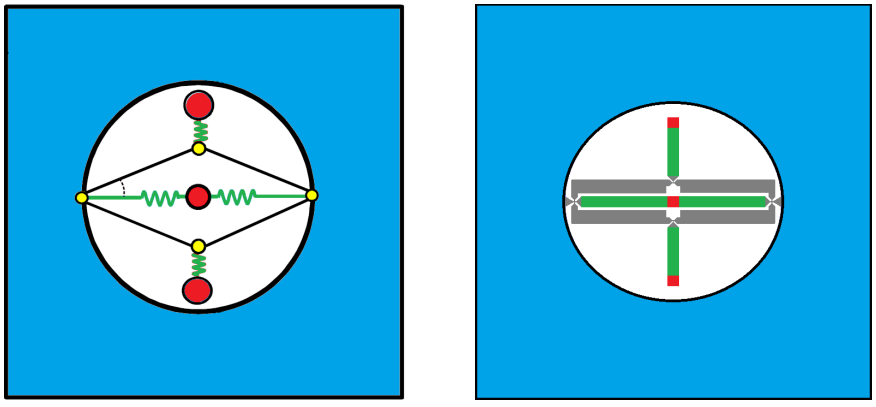

(a) (b)

Figure 6.1: Double negative unit cell design by Sridhar *et al.* [32]. a) Original unit cell design from paper. b) Adapted unit cell to support 2D analysis in COMSOL.

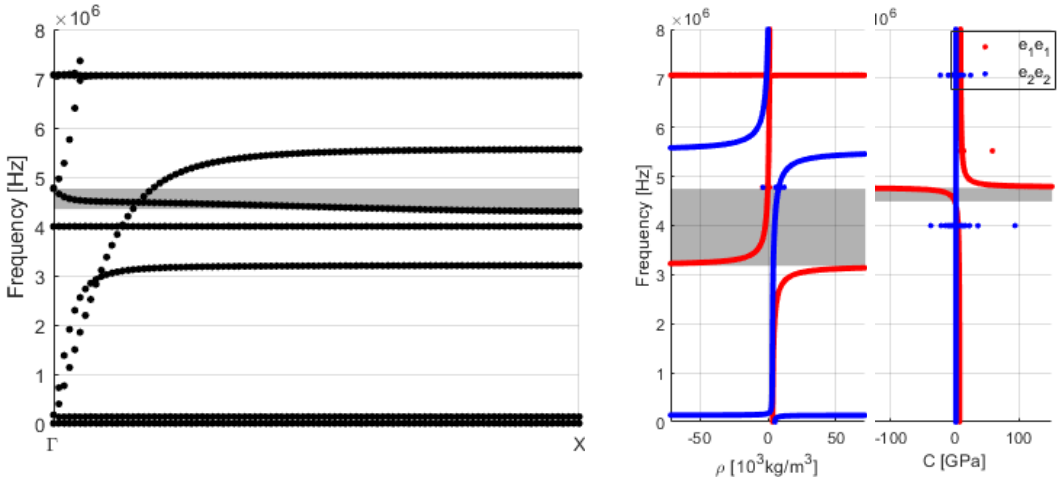

(a) (b) (c)

Figure 6.2: Unit cell performance for a certain frequency range. a) Band diagram, double negative regime highlighted by the grey area; b) effective density, and c) effective stiffness. The negative frequency regime highlighted with the grey areas.

The unit cell consists of a matrix medium material (blue) with a void (white), in this void a certain structure is placed. The red and green domains represent heavy masses and springs respectively. In the model of Fig. 6.1a, the springs are connected to hinges which are interconnected by rods. In the adapted model these rods are replaced by rigid domains with a negligible mass. At the locations of the hinges the material domains are connected by only one node, simulating a hinge and acquiring an equal structure as designed by Sridhar *et al.* [32]. The material properties of the adapted unit cell of Fig. 6.1b are provided in App. C.1. It must be noted that in order to get the unit cell with double negative properties, fictive material properties are produced. Especially for the rigid domains, since these do have a high Young's modulus but do not add to the total mass of the structure.

The negative effective mass and negative effective stiffness of the unit cells are achieved by redirecting a horizontally propagating wave into a vertically propagating wave. This is possible due to the connection of the top and bottom masses by rods to the left and right side; a horizontal displacement of the rods will result in a vertical displacement of the two outer masses. The actual displacement of the unit cells at certain frequencies is visualised in App. C.2. The phenomenon where only the outer masses are in resonance is one of the eigenmodes of the unit cell. At the frequencies for which this eigenmode is actuated, the double negative properties arise. The occurrence of the negative effective mass and effective stiffness can be seen in Figs. 6.2b and 6.2c respectively. The frequency range for which the negative properties arise are highlighted by the grey areas. The double negative properties can also be derived from the band diagram, the double negative band is characterised by its negative slope, this is highlighted by the grey area in Fig. 6.2a. This negative slope means the group velocity is negative at this point, which is the reason the negative refraction can take place.

6.2 Double Negative Metamaterial

Now the dynamical performance of the unit cell is evaluated. To do so, the unit cells are implemented in the coating layer.

First, it is tested whether the negative refraction found in the paper by Sridhar *et al.* [32] can be replicated using the unit cell of Fig. 6.1b modelled in COMSOL. The structure used for this evaluation is visualised in Fig. 6.3a, and consists of trapezium metamaterial domain with an

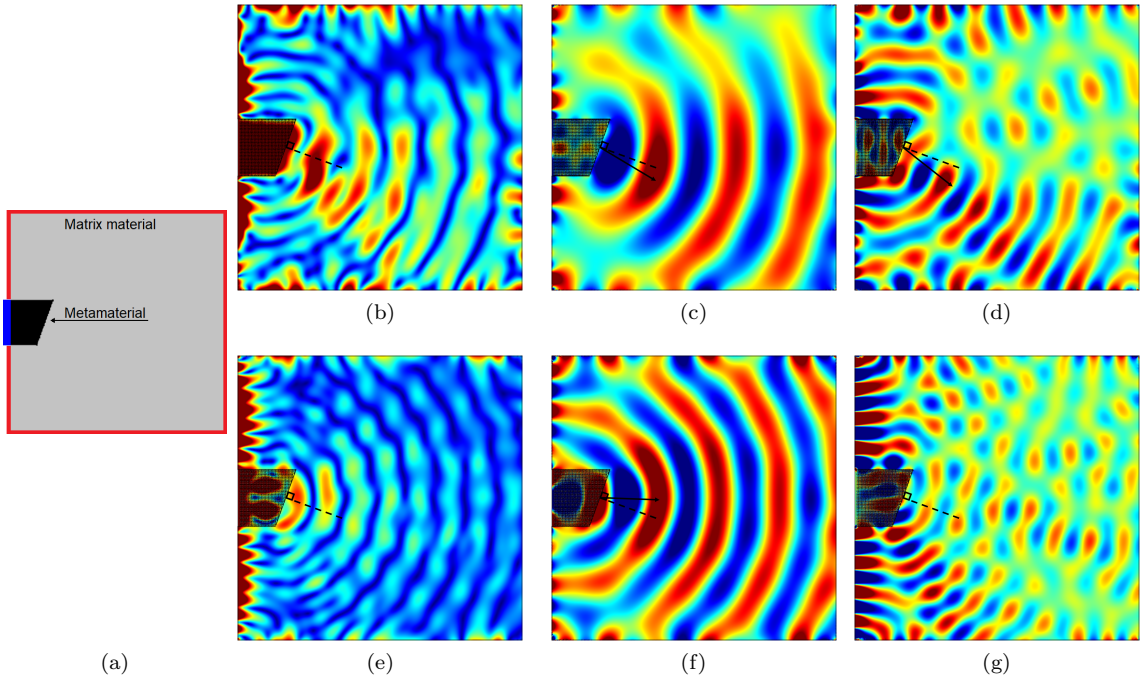

Figure 6.3: Results of a double negative metamaterial structure for an imposed harmonic displacement. a) Sketch of problem setup in COMSOL. b-d) Metamaterial results; total displacement field (b), longitudinal wave field (c) and shear wave field (d). e-g) Matrix material with voids results (as reference); total displacement field (e), longitudinal wave field (f) and shear wave field (g).

imposed harmonic normal displacement on one side of the domain (blue). On the other sides of the trapezium the matrix material of the metamaterial extends into a larger domain. On the sides of the structure a PML is modelled (red), attenuating the propagating waves. The metamaterial domain is 40 unit cells in height and width, with a 20 degrees angle on the side of the matrix material. The double negative unit cells are implemented horizontally, in line with the excited edge (blue). The matrix material domain is 200×200 unit cells in size. The results from this evaluation are shown in the remaining figures of Fig. 6.3. The top three figures show the results of the total displacement, longitudinal wave and shear wave respectively. These results are compared to the results for a reference coating, where the coating domain is modelled as the matrix material containing voids, the bottom three figures.

The shear wave coming from the metamaterial coating, Fig. 6.3d, is clearly more prominent in the negative refraction direction of the trapezium. Whereas the reference structure in Fig. 6.3g does not show a preferred direction at all, the wave is more or less evenly distributed over the domain. The same kind of propagation can be seen for the longitudinal wave of the reference structure; there is no preferred propagation direction. However, the longitudinal wave of the metamaterial coating does show a preferred direction. But this time the negativity of the wave is not that clear, this is because there is a splitting into a longitudinal wave propagating straight through the metamaterial (horizontal) and a negative refracted wave, indicated by the arrow. These two wave fields translate to the total displacement fields of Figs. 6.3b and 6.3e. Indeed, for an displacement normal to one side of a triangular coating layer, the propagating refracted wave has a negative angle. It must be noted that a considerable amount of unit cells is needed to pick up on the negative refraction angle occurring. Meaning that the estimated coating thickness of 3-5 consecutive ordinary resonating unit cells will not be sufficient when a double negative acoustic metamaterial is considered.

A comparable evaluation can be executed to assess whether the unit cells can also produce a

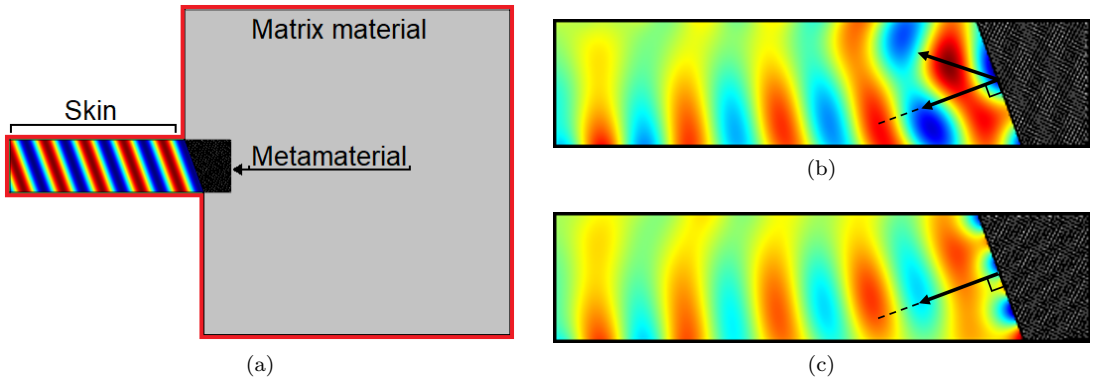

Figure 6.4: Results of a double negative metamaterial structure for an incident prescribed wave from a skin layer. a) Sketch of problem setup in COMSOL. b) Reflected wave for an wave incident on a metamaterial layer. c) Reflected wave for an wave incident on a matrix material layer containing voids (as reference).

negative reflection. Since the unit cell clearly shows a negative refraction, this may possibly mean a negative reflection can be achieved as well. To do this evaluation, the structure of Fig. 6.4a is considered. The structure consists of a skin domain on the left which is connected to the trapezium metamaterial domain, this trapezium is surrounded by a large domain with the properties of the matrix material, with the purpose of reducing boundary effects. The metamaterial domain is 42.6 unit cells wide and 48.4 unit cells in height, with a cut out to obtain the 20 degree angle trapezium. The double negative unit cells are implemented under an angle of 20 degrees, in line with skin-metamaterial interface. The large matrix material domain is 300×300 unit cells in size with a cut out to be in line with the cut out of the trapezium domain. The red edges indicate the edge is connected to a PML (perfectly matched layer). On the skin domain a pressure wave is applied which is propagating towards the coating domain, normal to the boundary of the coating domain. For an ordinary material domain this would imply that the reflected wave will be normal to this boundary as well. But when the domain has double negative properties, this angle is expected to change. In Figs. 6.4b and 6.4c the reflected pressure waves of these two situations are depicted; In Fig. 6.4b the domain contains double negative unit cells, in Fig. 6.4c the domain is modelled as the matrix material containing voids.

It can be seen that there is a significant difference between using a double negative metamaterial and using an ordinary material with voids. The reflected pressure field from the ordinary material shows a pressure wave travelling normal to the boundary, indicating the direction of the wave is unchanged. For the metamaterial with double negative properties this same wave is visible as well, however there is another wave reflected from the boundary. It seems indeed to be the case that the direction of the reflected wave has changed with respect to its expected angle of reflection.

There are however a couple of remarks on the above statement. First of all, the double negativity of the unit cell only exists for an incident wave normal to the boundary. When the incident angle is under a certain angle, the negative slope band in the band diagram is no more visible, this is also shown in App. C.2. Consequently, it is not possible to get a negative reflection for an incident wave not normal to the skin-coating interface, which is the case for ultrasound needle guidance. Alternatively, the unit cells have to be rotated corresponding to the incident angle, which is not practical. The original problem setup can therefore not be achieved. The second remark is that in the current configuration of Fig. 6.4a the incident wave is normal to the coating boundary, which does not comply with the actual problem definition. In the current situation the incident wave is normal to the boundary, which implies the source is normal to this boundary as well. Resulting in the optimal reflection of the incident wave to be normal to the boundary too. Therefore the coating with voids has strictly speaking a more optimal reflection than the coating with double negative properties.

Taking the remarks on the obtained results into consideration it can be concluded that the considered double negative metamaterial is not suited for improving the reflection of needle surfaces. However, it is demonstrated that the reflection angle can be manipulated using the double negative unit cells. With the knowledge coming from the above evaluation, it is not possible to give a conclusive judgement on whether it is possible to alter the reflection angle for incident waves under an angle. A different unit cell has to be designed that can handle rotated incident waves. Also, a unit cell with more realistic material properties would ease the next step of bringing the metamaterial coating to practice.

Conclusions

A needle is often difficult to visualise with ultrasound imaging guidance. The main objective of this study was to improve the visibility of this needle. To meet this objective, the current field of needle coatings is investigated and a thorough study about locally resonant acoustic metamaterials is performed.

From the research into the current field of techniques available to improve the ultrasound imaging of needles it can be concluded that according to medical professionals, needles coated with a polymer give the best ultrasound image. When looking into patented structures for polymer coating of needles, it became apparent that most patents focus on polymer coatings containing voids. This coating is used as the most advanced technique, however, the exact composition of the coatings concealed by the manufacturers. In the state of the art, there is no record of any patent for the implementation of resonant particles in the coating. This unexplored ultrasound enhancing technique was elaborated on in this report.

The materials and dimensions of a Locally Resonant Acoustic Metamaterial can be selected to have the required behaviour for a certain frequency range. The designed LRAM consisted of tungsten core particles coated with a rubber embedded in a polyethylene matrix material. When the frequency band diagram of this metamaterial is evaluated it can be seen that the first band gap occurs between 4.7 and 10.5 MHz. Next, this LRAM is implemented in a skin-coating-needle structure to evaluate the actual reflection factor of the structure. Within the limits of the band gap, a complete reflection can be achieved when the number of consecutive unit cells is sufficient. For the two-dimensional case this means that the coating must be at least three unit cells thick. For the three-dimension case, more unit cells are necessary to achieve a proper frequency range with complete reflection; five to seven unit cells would suffice. The volume fraction has a great influence on the reflection factor as well. When the volume fraction is too low, the reflection factor will immediately drop significantly after the start of the band gap. For a volume fraction of $f = 0.4$ for the two-dimensional case, this phenomenon will be limited. For the three-dimensional metamaterial the volume fraction must at least be $f = 0.4$ as well. Lastly, the distribution of the particles in the matrix material does not influence the reflection factor within the band gap. This allows for randomly distributed particles, which is ideal for practical applications. A comparison between the metamaterial coating and the coating containing voids shows that the LRAM definitely performs better. Therefore it can be concluded that the objective of improving the visibility of the needle is met.

Even when the needle is visualised under an angle, the metamaterial coating will outperform the coating containing voids. However, the angle of the reflected wave is not changed, which means the wave is not directed back towards the probe yet. To obtain this negative reflection angle, a structure used for obtaining a negative refraction is implemented. With this structure it is possible to manipulate the reflected wave using double negative effects of the metamaterial. However, the setup used in this study does not comply with a practical setup for an actual implementation as a coating. Therefore, the double negative metamaterial proposed in this study is not suited for improving the reflection of needle surfaces. But the application of a comparable metamaterial might be promising since it is demonstrated that the reflection angle can be manipulated using the double negative unit cells. For future work, it would be interesting to develop a different kind of double negative metamaterial, designed to actually manipulate the reflection angle in the direction of the probe.

Bibliography

[1] R.A. Adams and C. Essex. *Calculus: A complete course*, chapter 9.2: Infinite series. Pearson, 2013. 12

[2] K. Aki and P.G. Richards. *Quantitative seismology*, chapter 4. Elastic waves from a point dislocation source. In [3], 1980. 17

[3] K. Aki and P.G. Richards. *Quantitative seismology.* W.H. Freeman and company, 1980. 55

[4] K. Aki and P.G. Richards. *Quantitative seismology*, chapter 5. Plane waves in homogenious media and their reflection and transmission at a plane boundary. In [3], 1980. 61

[5] L.M. Brekhovskikh. *Waves in layered media*, chapter I. Plane waves in discretely layered media. Academic Press, 1980. 12, 15, 16, 19, 60, 61, 62

[6] L.M. Brekhovskikh and O.A. Godin. *Acoustics of layered media I*, chapter 1. Basic equations of wave processes in fluids and solids. In [7], 1990. 18

[7] L.M. Brekhovskikh and O.A. Godin. *Acoustics of layered media I.* Springer-Verlag, 1990. 55

[8] L.M. Brekhovskikh and O.A. Godin. *Acoustics of layered media I*, chapter 4. Plane-wave reflection from the boundaries of solids. In [7], 1990. 61, 62

[9] I.M. Cazacu, A.A.L. Chavez, A. Saftoiu, P. Vilmann, and M.S. Bhutani. A quarter century of EUS-FNA: Progress, milestones, and future directions. *Endosc. Ultrasound*, 7(3):141–160, 2018. 3

[10] L.A. Couvillon and T.J. Teo. Ultrasound coating for enhancing visualization of medical device in ultrasound images, April 7 2005. US20050074406A1. 4, 5

[11] P.A. Deymier. *Acoustic Metamaterials and Phononic Crystals*, chapter Chapter 1, Introduction to phononic crystals and acoustic metamaterials. In [12], 2013. 26

[12] P.A. Deymier. *Acoustic Metamaterials and Phononic Crystals.* Springer, 2013. 55, 56

[13] C. Eder. Medical devices with ultrasound-guided navigation ease needle placement for healthcare professionals, May 2017. 1

[14] H.H. Huang, C.T. Sun, and G.L. Huang. On the negative effective mass density in acoustic metamaterials. *Int. J. Eng. Sci.*, 47:610–617, 2009. 27, 28

[15] M.L. Jones, J. Uyeno, and G.E. Altieri. Echogenic coating, January 14 2003. US6506156B1. 4, 5

[16] H. Kolsky. *Stress waves in solids.* Dover Publications, 1963. 9, 59

[17] A.O. Krushynska, V.G. Kouznetsova, and M.G.D. Geers. Towards optimal design of locally resonant acoustic metamaterials. *J. Mech. Phys. Solids*, 71:179–196, 2014. 32

[18] Y. Lai, Y. Wu, P. Sheng, and Z. Zhang. Hybrid elastic solids. *Nat. Mater.*, 10:620–624, 2011. 47

[19] Y. Li, Z. Jiang, R. Li, B. Liang, X. Zou, L. Yin, and J. Cheng. Experimental Realization of Full Control of Reflected Waves with Subwavelength Acoustic Metasurfaces. *Phys. Rev. Appl.*, 2:064002, 2014. 25

[20] B. Liu, B. Ren, J. Zhao, X. Xu, Y. Feng, W. Zhau, and Y. Jiang. Experimental realization of all-angle negative refraction in acoustic gradient metasurface. *Appl. Phys. Lett.*, 111:221602, 2017. 25

[21] B. Liu, J. Zhao, X. Xu, W. Zhao, and Y. Jiang. All-angle Negative Refection with An Ultrathin Acoustic Gradient Metasurface: Floquet-Bloch Modes Perspective and Experimental Verifcation. *Sci. Rep.-UK*, 7:13852, 2017. 25

[22] X.N. Liu, G.K. Hu, L.G. Huang, and S.T. Sun. An elastic metamaterial with simultaneously negative mass density and bulk modulus. *Appl. Phys. Lett.*, 98(251907), 2011. 47

[23] Z. Liu, C.T. Chan, and P Sheng. Analytic model of phononic crystals with local resonances. *Phys. Rev. B*, 71(014103), 2005. 27

[24] Z. Liu, X. Zhang, Y. Mao, Y.Y. Zhu, Z. Yang, C.T. Chan, and P. Sheng. Locally resonant sonic materials. *Science*, 289(5485):1734–1736, 2000. 26, 27

[25] T.D. Mast. Empirical relationships between acoustic parameters in human soft tissues. *Acoust. Res. Lett. Onl.*, 1:37, 2000. 10, 32

[26] J. Mei, G. Ma, M. Yang, J. Yang, and P. Sheng. *Acoustic Metamaterials and Phononic Crystals*, chapter Chapter 5, Dynamic mass density and acoustic metamaterials. In [12], 2013. 27

[27] V. Narayanamurti, H. L. Strmer, M. A. Chin, A. C. Gossard, and W. Wiegmann. Selective Transmission of High-Frequency Phonons by a Superlattice: The 'Dielectric' Phonon Filter. *Phys. Rev. Lett.*, 43(27):2012–2015, 1979. 26

[28] L. Partika. Instrument having enhanced ultrasound visibility, January 24 1995. US5383466A. 4, 5

[29] M.M. Sigalas and E.N. Economou. Elastic and acoustic wave band structure. *J.Sound Vib.*, 158(2):377–382, 1992. 26

[30] M.M. Sigalas and E.N. Economou. Band structure of elastic waves in two dimensional systems. *Solid State Commun.*, 86(3):141–143, 1993. 26

[31] A. Sridhar, V.G. Kouznetsova, and M.G.D. Geers. A semi-analytical approach towards plane wave analysis of local resonance metamaterials using a multiscale enriched continuum description. *Int. J. Mech. Sci.*, 133:188–198, 2017. 34, 41

[32] A. Sridhar, L. Liu, V.G. Kouznetsova, and M.G.D. Geers. Homogenized enriched continuum analysis of acoustic metamaterials with negative stiffness and double negative effects. *J. Mech. Phys. Solids*, 119:104–117, 2018. 17, 47, 48, 67

[33] T.L. Szabo. *Diagnostic ultrasound imaging: inside out*, chapter 3. Acoustic wave propagation. Academic Press, 2014. 7, 8, 9

[34] S.J. Tang et al. EUS Needle Identification Comparison and Evaluation study (with videos). *Gastrointest. Endosc.*, 84(3):424–433, 2016. 3

[35] S.M. Tavakoli, A.J.C. Kellar, D Nassiri, and A.E. Joseph. A novel polymeric coating for enhanced ultrasound imaging of medical devices. In *Antec 2001*. CRC Press, May 2001. 5

[36] M.R. Violante, R.J. Whitbourne, J.F. Lanzafame, and M. Lydon. Echogenic coatings with overcoat, June 12 2007. US7229413B2. 1, 4, 5

[37] R. Zhu, X.N. Liu, G.K. Hu, C.T. Sun, and G.L. Huang. Negative refraction of elastic waves at the deep-subwavelength scale in a single-phase metamaterial. *Nat. Commun.*, 5(5510), 2014. 47

Appendix A

Wave Evaluation

A.1 Wave Speed

Firstly, a stress wave in a perfectly elastic medium is considered. To obtain the equations of motion for an elastic medium, an infinitesimal rectangular parallelepiped is concerned. On every face of this element a force is acting, this force can be decomposed into three separate forces; a displacement and a shear in the two remaining directions. These forces can be composed into a force in the x, y and z-direction. The resultant force in the x-direction can be composed to [16]:

$$F_x = \left(\frac{\partial \sigma_{xx}}{\partial x} + \frac{\partial \sigma_{xy}}{\partial y} + \frac{\partial \sigma_{xz}}{\partial z} \right) \delta x \delta y \delta z. \tag{A.1}$$

By Newton's second law of motion, when body forces are neglected, this will be equal to

$$F_x = (\rho \ \delta x \delta y \delta z) \frac{\partial^2 u_x}{\partial t^2}, \tag{A.2}$$

where u_x is the displacement of the element in x-direction. With this the equations of motion can be constructed a way that these equations hold for every stress-strain behaviour of the medium:

$$\rho \frac{\partial^2 u_x}{\partial t^2} = \frac{\partial \sigma_{xx}}{\partial x} + \frac{\partial \sigma_{xy}}{\partial y} + \frac{\partial \sigma_{xz}}{\partial z}. \tag{A.3}$$

To this equation, Hooke's law applied. Since the material is isotropic and elastic, the generalised form of Hooke's law reduces to:

$$\begin{cases} \sigma_{ii} = \lambda \mathrm{tr}\,(\epsilon) + 2\mu\epsilon_{ii} & \\ \sigma_{ij} = \mu\epsilon_{ij} & (i \neq j)\,, \end{cases} \tag{A.4}$$

where ϵ is the strain of the element. The parameters λ and μ are Lamé constants, defining the elastic behaviour of the isotropic material. Lamé constant μ is also known as the shear modulus. As Hooke's law is applied to Eq. (A.3), the equation of motion in the x-direction becomes:

$$\rho \frac{\partial^2 u_x}{\partial t^2} = \frac{\partial}{\partial x} \left(\lambda \mathrm{tr}\,(\epsilon) + 2\mu\epsilon_{xx} \right) + \frac{\partial}{\partial y} \left(\mu\epsilon_{xy} \right) + \frac{\partial}{\partial z} \left(\mu\epsilon_{xz} \right) \tag{A.5}$$

For an infinitesimal rectangular parallelepiped, the expansions and strains can be written as:

$$\begin{cases} \epsilon_{xx} = \frac{\partial u_x}{\partial x} & \\ \epsilon_{xy} = \frac{\partial u_y}{\partial x} + \frac{\partial u_x}{\partial y} & \\ \epsilon_{xz} = \frac{\partial u_z}{\partial x} + \frac{\partial u_x}{\partial z}. & \end{cases} \tag{A.6}$$

When these equations are applied to Eq. (A.5) and the same trick is applied to the y and z-direction, the resulting equations are:

$$\begin{aligned}
\rho\frac{\partial^2 u_x}{\partial t^2} &= (\lambda+\mu)\frac{\partial \mathrm{tr}\,(\epsilon)}{\partial x} + \mu\nabla^2 u_x,\\
\rho\frac{\partial^2 u_y}{\partial t^2} &= (\lambda+\mu)\frac{\partial \mathrm{tr}\,(\epsilon)}{\partial y} + \mu\nabla^2 u_y,\\
\rho\frac{\partial^2 u_z}{\partial t^2} &= (\lambda+\mu)\frac{\partial \mathrm{tr}\,(\epsilon)}{\partial z} + \mu\nabla^2 u_z.
\end{aligned} \tag{A.7}$$

With the use of these equations of motion for an isotropic elastic material, the propagation of longitudinal and transverse waves through the medium can be calculated. If the three equations in Eq. (A.7) are differentiated to x, y and z respectively, the equations can be reduced to:

$$\rho\frac{\partial^2 \mathrm{tr}\,(\epsilon)}{\partial t^2} = (\lambda+2\mu)\,\nabla^2 \mathrm{tr}\,(\epsilon)\,, \tag{A.8}$$

this equation is referred to as the wave equation. From this equation propagation velocities can be derived: $c_1 = [(\lambda+2\mu)/\rho]^{\frac{1}{2}}$ is the velocity with which the change in density propagates through the medium (longitudinal waves). Since the bulk modulus $K = \lambda + \frac{2}{3}\mu$, the speed of the longitudinal waves through a solid can be written as: $c_1 = \left[\left(K+\frac{4}{3}\mu\right)/\rho\right]^{\frac{1}{2}}$. For liquids μ will be negligible, reducing the equation for the speed of longitudinal waves through a liquid medium to: $c_1 = [K/\rho]^{\frac{1}{2}}$.

Now, instead of differentiating the wave equation with respect to their direction, the second and third equation of Eq. (A.7) are differentiated to z and y respectively. Thus eliminating $\mathrm{tr}\,(\epsilon)$:

$$\rho\frac{\partial^2}{\partial t^2}\left(\frac{\partial u_z}{\partial y} - \frac{\partial u_y}{\partial z}\right) = \mu\nabla^2\left(\frac{\partial u_z}{\partial y} - \frac{\partial u_y}{\partial z}\right). \tag{A.9}$$

Here, $\left(\frac{\partial u_z}{\partial y} - \frac{\partial u_y}{\partial z}\right)$ is the rotation about the x-axis. The rotational waves propagate with a velocity of $c_2 = [\mu/\rho]^{\frac{1}{2}}$ (transverse waves). Since μ can be neglected for a liquid, there will be no transverse waves. For the y and z-axis, similar equations can be derived.

A.2 Analytical Derivation: Reflection from an Arbitrary Number of Solid Layers

For the analysis of a three layer interface including a solid layer, a general expression for a wave hitting an arbitrary number of solid layers is set up. In this general expression, the propagation of a longitudinal and shear wave in every layer can be related to the waves in the adjacent layers. The potentials ϕ and ψ, of the longitudinal and shear wave in every layer respectively, can be written as [5]:

$$\begin{aligned}
\phi &= \phi' e^{i\alpha z} + \phi'' e^{-i\alpha z}, \qquad \text{where } \alpha = \sqrt{k_L^2 - \xi^2}, \qquad k_L = \frac{\omega}{c_L},\\
\psi &= \psi' e^{i\beta z} + \psi'' e^{-i\beta z}, \qquad \text{where } \beta = \sqrt{k_S^2 - \xi^2}, \qquad k_S = \frac{\omega}{c_S},
\end{aligned} \tag{A.10}$$

where ϕ' and ψ' are the amplitudes of the reflected longitudinal and shear wave respectively, ϕ'' and ψ'' are the amplitudes of the incident longitudinal and shear wave respectively and k_L and k_S represent the wave number of the longitudinal and shear wave respectively. The parameter ξ is the horizontal component of the wave number of the incident wave, and is determined by the angle of incident. The angles of all waves in every medium are determined by using Snell's law, similarly to the previous analytical derivations.

The axis z is perpendicular to the interfaces, $z = 0$ is temporary positioned at the bottom boundary of a considered layer with thickness d, which means the top boundary of layer n is at $z = d$. The displacements and stresses of layer at $z = d$ can be expressed as u_x and u_z for the displacements and σ_{zx} and σ_{zz} for the stresses [5, 8]:

$$\begin{aligned} u_x &= \frac{\partial \phi}{\partial x} - \frac{\partial \psi}{\partial z}, \\ u_z &= \frac{\partial \phi}{\partial z} + \frac{\partial \psi}{\partial x}, \end{aligned} \tag{A.11}$$

$$\begin{aligned} \sigma_{zz} &= \lambda \left(\frac{\partial u_x}{\partial_x} + \frac{\partial u_z}{\partial z} \right) + 2\mu \frac{\partial u_z}{\partial z} = 2\xi\mu(\gamma\phi + i\frac{\partial \psi}{\partial z}), \\ \sigma_{zx} &= \mu \left(\frac{\partial u_x}{\partial z} + \frac{\partial u_z}{\partial x} \right) = -2\xi\mu(\gamma\psi - i\frac{\partial \phi}{\partial z}). \end{aligned} \tag{A.12}$$

where μ and λ are the Lamé constants and where $\gamma = \xi - k_S^2/2\xi$. Now u_x at the top layer, where $z = d$, is calculated to be:

$$u_x^{(n)} = i\xi\,\phi' e^{i\alpha z} + i\xi\,\phi'' e^{-i\alpha z} - i\beta\,\psi' e^{i\beta z} + i\beta\,\psi'' e^{-i\beta z}, \tag{A.13}$$

A similar solution can be found for the remaining stresses and displacements. Resulting in the following solution matrix [8]:

$$\begin{bmatrix} u_x^{(n)} \\ u_z^{(n)} \\ \sigma_{zz}^{(n)} \\ \sigma_{zx}^{(n)} \end{bmatrix} = \begin{bmatrix} i\xi & i\xi & -i\beta & i\beta \\ i\alpha & -i\alpha & i\xi & i\xi \\ 2\mu\xi\gamma & 2\mu\xi\gamma & -2\mu\xi\beta & 2\mu\xi\beta \\ -2\mu\xi\alpha & 2\mu\xi\alpha & -2\mu\xi\gamma & -2\mu\xi\gamma \end{bmatrix} \begin{bmatrix} \phi' e^{i\alpha z} \\ \phi'' e^{-i\alpha z} \\ \psi' e^{i\beta z} \\ \psi'' e^{-i\beta z} \end{bmatrix}. \tag{A.14}$$

At the lower interface, where $z = 0$, a similar set of equations can be derived. But first the displacements and stresses of two adjacent layers can be expressed using a transformation matrix expressed as $\mathbf{a}$ [5, 8]:

$$\begin{bmatrix} u_x^{(n)} \\ u_z^{(n)} \\ \sigma_{zz}^{(n)} \\ \sigma_{zx}^{(n)} \end{bmatrix} = \mathbf{a} \begin{bmatrix} u_x^{(n+1)} \\ u_z^{(n+1)} \\ \sigma_{zz}^{(n+1)} \\ \sigma_{zx}^{(n+1)} \end{bmatrix}, \tag{A.15}$$

where the elements of the matrix $\mathbf{a}$ are calculated to be [4, 5, 8]:

$$\begin{aligned} \mathbf{a}_{11} &= \mathbf{a}_{44} = 2\sin^2\theta_S \cos P + \cos 2\theta_S \cos Q, \\ \mathbf{a}_{12} &= \mathbf{a}_{34} = i\left(\tan\theta_L \cos 2\theta_S \sin P - \sin 2\theta_S \sin Q\right), \\ \mathbf{a}_{13} &= \mathbf{a}_{24} = i\sin\theta_S(\cos Q - \cos P)/\omega\rho c_S, \\ \mathbf{a}_{14} &= (\tan\theta_L \sin\theta_S \sin P + \cos\theta_S \sin Q)/\omega\rho c_S, \\ \mathbf{a}_{21} &= \mathbf{a}_{43} = i(2\cot\theta_L \sin^2\theta_S \sin P - \tan\theta_S \cos 2\theta_S \sin Q), \\ \mathbf{a}_{22} &= \mathbf{a}_{33} = \cos 2\theta_S \cos P + 2\sin^2\theta_S \cos Q, \\ \mathbf{a}_{23} &= (\cot\theta_L \sin\theta_S \sin P + \sin\theta_S \tan\theta_S \sin Q)/\omega\rho c_S, \\ \mathbf{a}_{31} &= \mathbf{a}_{42} = -2i\omega\rho c_S \sin\theta_S \cos 2\theta_S(\cos Q - \cos P), \\ \mathbf{a}_{32} &= -\omega\rho c_S(\tan\theta_L \cos^2 2\theta_S \sin P + \sin^2 2\theta_S \tan\theta_S \sin Q)/\sin\theta_S, \\ \mathbf{a}_{41} &= -\omega\rho c_S[4\cot\theta_L \sin^3\theta_S \sin P + (\cos^2 2\theta_S/\cos\theta_S)\sin Q]. \end{aligned} \tag{A.16}$$

In these equations, $P = \alpha d$ and $Q = \beta d$. When a structure consists of n layers (excluding the incident layer), an $\mathbf{a}$ matrix for layer (2) up to $(n-1)$ needs to be constructed. Multiplication of

these matrices results in matrix **A**, which is a measure for the propagation of the waves through the complete structure of n layers [5, 8]:

$$\begin{bmatrix} u_x^{(1)} \\ u_z^{(1)} \\ Z_z^{(1)} \\ Z_x^{(1)} \end{bmatrix} = \mathbf{A} \begin{bmatrix} u_x^{(n)} \\ u_z^{(n)} \\ Z_z^{(n)} \\ Z_x^{(n)} \end{bmatrix}. \tag{A.17}$$

Now the reflection factor and transmission factor can be determined. For this, $z = 0$ is set on the boundary between the last and second to last medium. The total thickness of all layers is denoted by $H = d^{(2)} + \cdots + d^{(n)}$. Then the total field of the incident and reflected sound waves in the upper layer can be written as [5, 8]:

$$\phi^{(0)} = e^{-\alpha^{(0)}(z-H)} + RFe^{i\alpha^{(0)}(z-H)}, \qquad \text{where } z \geq H, \tag{A.18}$$

where $\alpha^{(0)} = k_L^{(0)} \cos\theta_L^{(0)}$. In the last layer there will only be a transmitted wave; there is no more reflection in the last layer. The potentials in this layer can be written as:

$$\begin{aligned} \phi^{(n)} &= TF_L e^{-ik_L^{(n)} z \cos\theta_L^{(n)}}, \\ \psi^{(n)} &= TF_S e^{-ik_S^{(n)} z \cos\theta_S^{(n)}}. \end{aligned} \tag{A.19}$$

RF, TF_L and TF_S can be found from the conditions on the boundary of the media 0 and 1 [5]:

$$z = H, \qquad u_z^{(0)} = u_z^{(1)}, \qquad Z_z^{(0)} = Z_z^{(1)}, \qquad Z_x^{(0)} = Z_x^{(1)} = 0. \tag{A.20}$$

If these conditions are implemented for the solutions of $u_z^{(1)}$, $Z_z^{(1)}$ and $Z_x^{(1)}$ of Eq. (A.17), a solution for the top layer 0 can be constructed:

$$\begin{aligned} u_z^{(0)} &= A_{21}u_x^{(n)} + A_{22}u_z^{(n)} + A_{23}Z_z^{(n)} + A_{24}Z_x^{(n)}, \\ Z_z^{(0)} &= A_{31}u_x^{(n)} + A_{32}u_z^{(n)} + A_{33}Z_z^{(n)} + A_{34}Z_x^{(n)}, \\ 0 &= A_{41}u_x^{(n)} + A_{42}u_z^{(n)} + A_{43}Z_z^{(n)} + A_{44}Z_x^{(n)}. \end{aligned} \tag{A.21}$$

The last equation can be solved for $u_x^{(n)}$ and substituted into the first two equations:

$$\begin{aligned} u_z^{(0)} &= M_{22}u_z^{(n)} + M_{23}Z_z^{(n)} + M_{24}Z_x^{(n)}, \\ Z_z^{(0)} &= M_{32}u_z^{(n)} + M_{33}Z_z^{(n)} + M_{34}Z_x^{(n)}, \end{aligned} \tag{A.22}$$

where:

$$M_{ik} = A_{ik} - \frac{A_{i1}A_{4k}}{A_{41}}, \qquad i,k = 2,3,4. \tag{A.23}$$

Now Eq. (A.17) is considered again, but now this equation is filled in with the values of the displacements and stresses as a function of the reflection and transmission factors. Using Eqs. (A.11), (A.12), (A.18) and (A.19) and looking at the situation where $z = H$ or $z = 0$, Eq. (A.17) becomes [8]:

$$\begin{bmatrix} i\xi(1+RF) \\ i\alpha^{(0)}(RF-1) \\ -\omega^2\rho^{(0)}(1+RF) \\ 0 \end{bmatrix} = \mathbf{A} \begin{bmatrix} i\xi TF_L + i\beta^{(n)}TF_S \\ -i\alpha^{(n)}TF_L + i\xi TF_S \\ 2\mu^{(n)}\xi(\gamma^{(n)}TF_L + \beta^{(n)}TF_S) \\ 2\mu^{(n)}\xi(\alpha^{(n)}TF_L - \gamma^{(n)}TF_S) \end{bmatrix}. \tag{A.24}$$

Now a relation for the reflection factor RF can be derived:

$$RF = \frac{Z^{(in)} - Z^{(0)}}{Z^{(in)} + Z^{(0)}} \tag{A.25}$$

where

$$\begin{aligned} Z^{(in)} &= \frac{iZ_z^{(0)}}{\omega u_z^{(0)}} = -\frac{N_3}{i\omega N_2}, \\ Z^{(0)} &= \frac{\rho^{(0)} c_L^{(0)}}{\cos\theta_L^{(0)}}, \end{aligned} \tag{A.26}$$

where, for the total input impedance Z_{in}:

$$\begin{aligned} N_j =& \alpha^{(n)} M_{j2} - i\omega^2 \rho^{(n)} (\cos 2\theta_S^{(n)} M_{j3} - (c_S^{2(n)}/c_L^{2(n)}) \sin 2\theta_L^{(n)} M_{j4}) \\ & - (\xi M_{j2} - i\omega^2 \rho^{(n)} (\sin 2\theta_S^{(n)} M_{j3} + \cos 2\theta_S^{(n)} M_{j4})) \frac{TF_S}{TF_L}, \qquad j = 2, 3 \end{aligned} \tag{A.27}$$

the fraction of TF_S/TF_L can be derived from the last equation of Eq. (A.21), substituted with $z = 0$ of Eq. (A.24):

$$\frac{TF_S}{TF_L} = -\frac{\xi A_{41} - \alpha^{(n)} A_{42} + i\omega^2 \rho^{(n)} \cos 2\theta_S^{(n)} A_{43} - i\omega^2 \rho^{(n)} (c_S^{2(n)}/c_L^{2(n)}) \sin 2\theta_L^{(n)} A_{44}}{k_S^{(n)} \cos\theta_S^{(n)} A_{41} + \xi A_{42} - i\omega^2 \rho^{(n)} \sin 2\theta_S^{(n)} A_{43} - i\omega^2 \rho^{(n)} (c_S^{2(n)}/c_L^{2(n)}) \sin 2\theta_L^{(n)} A_{44}}. \tag{A.28}$$

The transmission factor TF can be obtained from the first equation of Eq. (A.21), taking Eq. (A.24) in account:

$$TF_L = \frac{\rho^{(n)}}{\rho^{(0)}} \frac{2\alpha^{(0)} Z^{(0)}}{Z^{(in)} + Z^{(0)}} \frac{1}{T}, \tag{A.29}$$

where:

$$\begin{aligned} T =& -\xi A_{21} + \alpha^{(n)} A_{22} - i\omega^2 \rho^{(n)} \cos 2\theta_S^{(n)} A_{23} + i\omega^2 \rho^{(n)} (c_S^{2(n)}/c_L^{2(n)}) \sin 2\theta_L^{(n)} A_{24} \\ & + \frac{TF_S}{TF_L} (-k_S^{(n)} \cos\theta_S^{(n)} A_{21} - \xi A_{22} + i\omega^2 \rho^{(n)} \sin 2\theta_S^{(n)} A_{23} + i\omega^2 \rho^{(n)} \cos 2\theta_S^{(n)} A_{24}). \end{aligned} \tag{A.30}$$

Now a complete method is derived for the reflection and transmission factors of a wave incident on a solid structure of an arbitrary number of layers.

Appendix B

LRAM Reflection

B.1 Reflection factors for 2D structures

From Fig. B.1 it can be seen that the dips in the reflection factor will not take place in the band gap domain. No matter how many unit cells are used.

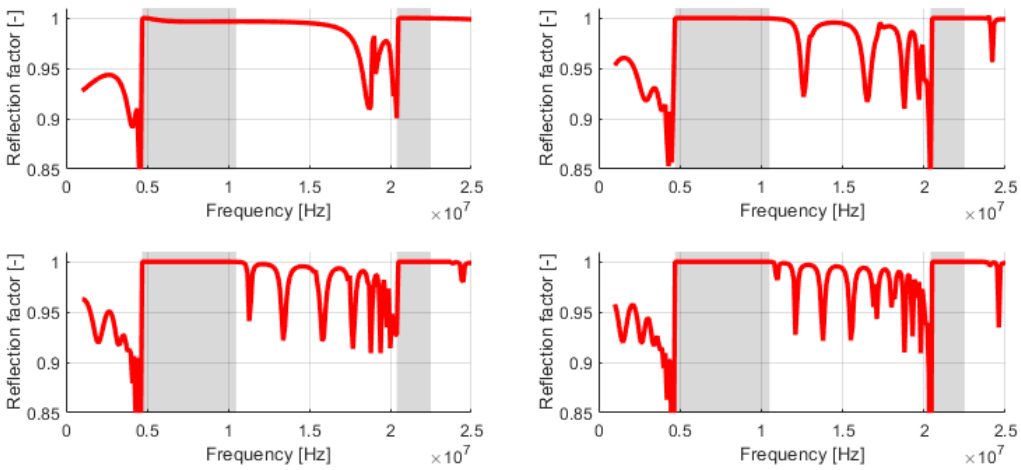

Figure B.1: Reflection factor for a wave with normal incident on a coating, no reflection possible at the end of the coating layer. Comparison of a LRAM coating and a homogenised coating. For a LRAM consisting of: a) 3 unit cell, b) 9 unit cells, c) 15 unit cells, d) 21 unit cells. The grey areas highlight the band gaps of the unit cell.

Appendix C

Double Negative Metamaterial

C.1 Unit cell dimension and properties

The unit cell that is designed is based on the principles of the model by Sridhar *et al.* [32]. The model is scaled to match the frequency regime relevant for ultrasound imaging. The material properties and unit cell dimensions used in the evaluations in this report are given in Tables C.1 and C.2. The grey areas in Fig. 6.1b that represented the rigid domains are build up out of a material with an unusual high Young's modulus and a negligible mass.

Table C.1: Dimensions of double negative unit cell.

Unit cell dimensions	
Unit cell width	10 [μm]
Void radius x	2.75 [μm]
Void radius y	2.5 [μm]
'Hinge' angle	10.8 [deg]
Resonator width	0.208 [μm]
Resonator length side	1.25 [μm]
Resonator length mid	2.23 [μm]

Table C.2: Material properties of double negative unit cell.

Unit cell material properties	
Mass matrix	0.16075 [mg]
Side masses	0.0785 [mg]
Middle mass	0.19625 [mg]
Young's modulus resonator sides	602 [MPa]
Young's modulus resonator mid	428 [MPa]

C.2 Double negative unit cell dynamics

In this section, the displacement of the double negative unit cell is provided for different bands in the frequency band diagram of Fig. 6.2a. After that, the frequency band diagram for a rotated incident wave of 20 deg on the double negative unit cell is provided.

The mode shapes show similar displacements of the unit cell as for the ordinary negative mass metamaterial. Figs C.1a and C.1b show the unit cell displacement for the longitudinal and shear band respectively. The horizontal band below the double negative band is caused by a rotational resonance. This resonance is visualised in Fig. C.1c. In Fig. C.1d the unit cell displacement of

the double negative band is visualised. The difference with the shear displacement, Fig. C.1b is that the energy is directed to only one side of the unit cell. This will result in the excitement of the unit cell in the vertical direction, this new wave will cause for a manipulation of the refracted wave.

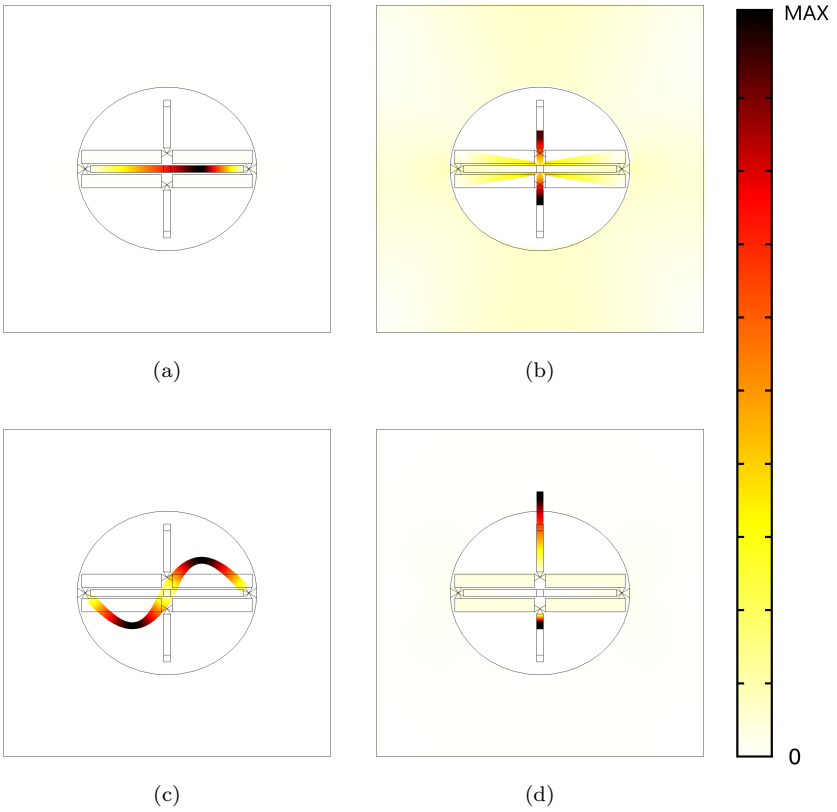

Figure C.1: Mode shapes of some local resonant eigenmodes of the unit cell with double negative properties. The Colours range from no displacement to the maximum displacement, which can be different for every mode shape.

From the frequency band diagram for the double negative metamaterial with a rotated wave vector it can be seen that the double negative band has split. The bands for the shear wave and for the double negativity interfere, this disrupts the functioning of the double negativity of the metamaterial.

Figure C.2: Frequency band diagram of a double negative unit cell with a rotated incident wave of 20 degrees. The negative band has split.

Technische Universiteit
Eindhoven
University of Technology

Declaration concerning the TU/e Code of Scientific Conduct for the Master's thesis

I have read the TU/e Code of Scientific Conduct[i].

I hereby declare that my Master's thesis has been carried out in accordance with the rules of the TU/e Code of Scientific Conduct

Date

18-05-2020

Name

Cas van der Vleuten

ID-number

0844042

Signature

Submit the signed declaration to the student administration of your department.

[i] See: http://www.tue.nl/en/university/about-the-university/integrity/scientific-integrity/
The Netherlands Code of Conduct for Academic Practice of the VSNU can be found here also.
More information about scientific integrity is published on the websites of TU/e and VSNU